Low-temperature oxidative removal of gaseous formaldehyde by an eggshell waste supported silver-manganese dioxide bimetallic catalyst with ultralow noble metal content

Kumar Vikrant [a], Ki-Hyun Kim [a,*], Fan Dong [b,*], Philippe M. Heynderickx [c, d,*], Danil W. Boukhvalov [e, f]

[a] Department of Civil and Environmental Engineering, Hanyang University, 222 Wangsimni-Ro, Seoul 04763, Republic of Korea

[b] Yangtze Delta Region Institute (Huzhou) & Institute of Fundamental and Frontier Sciences, University of Electronic Science and Technology of China, Huzhou 313001, China

[c] Center for Environmental and Energy Research (CEER), Engineering of Materials via Catalysis and Characterization, Ghent University Global Campus, 119-5 Songdo Munhwa-ro, Yeonsu-gu, Incheon 406-840, Republic of Korea

[d] Department of Green Chemistry and Technology, Faculty of Bioscience Engineering, Ghent University, Coupure Links 653, B-9000 Ghent, Belgium

[e] College of Science, Institute of Materials Physics and Chemistry, Nanjing Forestry University, Nanjing 210037, China

[f] Institute of Physics and Technology, Ural Federal University, Mira Street 19, 620002 Yekaterinburg, Russia

Abstract

Under dark/low temperature (DLT) conditions, the oxidative removal of gaseous formaldehyde (FA) was studied using eggshell waste supported silver (Ag)-manganese dioxide (MnO_2) bimetallic catalysts. To assess the synergistic effects between the two types of metals, 0.03%-Ag-(0.5-5%)-MnO_2/Eggshell catalysts were prepared and employed for DLT-oxidation of FA. The steady-state FA oxidation reaction rate (mmol g^{-1} h^{-1}), when measured using 100 ppm FA at 80°C (gas hourly space velocity (GHSV) of 5,308 h^{-1}), varied as follows: Ag-1.5%-MnO_2/Eggshell-R (9.4) > Ag-3%-MnO_2/Eggshell-R (8.1) > Ag-1.5%-MnO_2/Eggshell (7.5) > Ag-5%-MnO_2/Eggshell-R (7.2) > Ag-1.5%-MnO_2/$CaCO_3$-R (6.8) > MnO_2-R (6) > Ag-0.5%-MnO_2/Eggshell-R (3.2) > Ag/Eggshell-R (2.6). Here, 'R' denotes hydrogen-based thermochemical reduction pretreatment. The temperature required for 90% FA conversion (T_{90}) at the same GHSV exhibited a contrary ordering: Ag/Eggshell-R (175°C) > Ag-0.5%-MnO_2/Eggshell-R (123°C) > Ag-5%-MnO_2/Eggshell-R (113°C) > MnO_2-R (99°C) > Ag-1.5%-MnO_2/Eggshell (96°C) > Ag-3%-MnO_2/Eggshell-R (93°C) > Ag-1.5%-MnO_2/Eggshell-R (77°C). The eggshell catalyst outperformed the commercial calcium carbonate variety due to the presence of defects in the former. The MnO_2 co-catalyst enhances the capture and activation of atmospheric oxygen (O_2) to boost the overall activity through rapid catalytic regeneration. Also, MnO_2 favorably captures the hydrogen of the adsorbed FA molecules to make the oxidation pathway thermodynamically more favorable.

***Keywords*:** Formaldehyde; Volatile organic compounds; Solid biowaste; Catalytic oxidation; Indoor air

***Corresponding Author:** kkim61@hanyang.ac.kr **(K.-H. Kim);** dongfan@uestc.edu.cn **(F. Dong);** philippe.heynderickx@ghent.ac.kr **(P.M. Heynderickx)**

1. Introduction

The presence of hazardous gaseous pollutants (e.g., volatile organic compounds (VOCs)) is generally related to their adverse impacts on human health [1-3]. Among various VOCs, formaldehyde (FA) has been considered a key target due to its high carcinogenicity [4, 5]. FA in the indoor air is liberated from various consumer goods such as furniture, cosmetics, and other products [6]. It is noted that FA in the ambient air is usually present in ppb or sub-ppm levels. However, its concentrations can reach several hundred ppm in industrial effluents as it is the key consumable in the manufacture of various products (e.g., textiles, pharmaceuticals, pesticides, artificial leather, organic chemicals, paints, adhesives, inks, and electronic equipment) [4, 6, 7]. In light of its potential as a human health hazard, the Occupational Safety and Health Administration has set a permissible FA exposure limit of 750 ppb (for an 8 h workday) [4].

In recent years, the techniques for low-temperature catalytic oxidation have been established to convert FA into carbon dioxide (CO_2) and water (H_2O) under dark/low temperature (DLT) conditions as an environmentally benign and reliable technique [8, 9]. The DLT catalytic oxidation of FA has typically been obtained by applying supported platinum (Pt) catalysts [10, 11]. Despite the high catalytic activities of Pt-based catalysts, their applications are often restricted in a practical sense due to their exorbitant cost [12, 13]. In this regard, the utility of silver (Ag) has been explored actively as an economical alternative to Pt to drive the DLT catalytic oxidation reactions of FA [13, 14].

As an alternative to the supported noble metal catalysts (SNMCs), inexpensive transition metal oxides such as manganese dioxide (MnO_2) have shown enhanced potential to drive the DLT oxidation reaction for FA [12, 15]. MnO_2 has been explored extensively as a suitable catalyst for VOC oxidation due to its various crystalline and amorphous phases, multiple oxidation states, and large oxygen storage capacity [12, 16, 17]. However, the catalytic oxidation efficacy of pristine MnO_2 is not good enough for specific targets (e.g., FA) if applied at low temperatures. Hence, its combination with noble metals (e.g., Ag) has been proposed as an effective option to overcome such limitations [12, 18]. For example, an Ag-potassium (K)/MnO_2 nanorod and a three-dimensional ordered mesoporous MnO_2 supported Ag catalyst were reported to exhibit effective oxidative removal of FA under the DLT conditions with the aid of the Ag-MnO_2 synergy [18, 19]. However, the alkali metal promoter, bulk MnO_2 supports, and high noble metal loadings (0.1-8.9 wt.%) were still needed for the Ag-MnO_2 catalysts to attain good FA oxidation performance at the DLT conditions [18, 19]. In light of such limitations, an attempt was made in the present research to validate the hypothesis whether the noble/non-noble metal oxides (e.g., Ag-MnO_2 prepared with an ultralow (e.g., < 0.05 wt.%) Ag fraction) loaded onto a support material can synergistically bring about FA oxidation with high catalytic activity.

With the backdrop of the circular economy, enormous efforts have been made to convert solid waste like spent eggshells into high-performance catalysts [20, 21]. Eggshell is essentially identical to calcite (biogenic calcium carbonate ($CaCO_3$)) with interwoven protein (glycoproteins and collagens)-rich membranes [13]. The presence of protein can help in the adsorption of noble metals during SNMC synthesis [13, 22, 24]. Due to its multifaceted advantages, global availability, and eco-friendliness, eggshell-based materials have been extensively applied in various environmental remediation fields (e.g., wastewater treatment and air quality management (AQM)) [21, 23, 25].

79 Likewise, the thermocatalytic oxidation of gaseous benzene has been examined by combining
80 eggshells with diverse metallic components such as Ag/Eggshell, Pt/Eggshell, and cobalt (II, III) oxide
81 (Co_3O_4)/Eggshell [13, 22, 23]. Our recent work explored the utility of K-Pt/Eggshell catalyst for the
82 DLT FA oxidation reaction [26]. Despite such efforts, the practical applications of eggshell waste-
83 based catalysts have only very rarely been made in treating VOCs. Also, although the FA oxidation
84 mechanism and pathway for SNMCs and MnO_2-based thermocatalysts are well established in the
85 literature, the effect of co-catalysts (e.g., Ag-MnO_2 synergy) in such a process remains largely
86 unknown [10, 12]. Furthermore, the use of a synergistic Ag-MnO_2 interface for the DLT FA oxidation
87 reaction has been rarely explored to date.

88 In this study, 0.03%-Ag-(0.5-5%)-MnO_2/Eggshell catalysts were prepared for the DLT FA
89 oxidation reaction in air. The optimum MnO_2 loading was determined by conducting a series of
90 oxidation tests to treat FA at DLT. Subsequently, the effect of process variables (e.g., catalyst mass
91 (m_{cat}; 30-120 mg), flow rate (50-500 mL min^{-1}), FA concentration (35-2,500 ppm), relative humidity
92 (RH; ~ 0-90%), and time-on-stream (TOS; 50 h)) was assessed using the best-performing catalyst for
93 FA oxidation. The FA oxidation pathway was determined using *in-situ* diffuse reflectance infrared
94 Fourier transform spectroscopy (DRIFTS). H_2 temperature-programmed reduction (TPR) experiments
95 gave information about the possible oxygen species on the surface catalyst. Furthermore, density
96 functional theory (DFT) simulations were employed to understand the surface phenomena, FA reaction
97 pathways, and associated mechanisms. We believe that the present study is the first report on both the
98 synthesis of Ag-MnO_2/Eggshell, and on testing its feasibility as a catalyst against VOCs (with the main
99 emphasis on FA in this work). Hence, the low-temperature oxidation of gaseous FA (under a
100 continuous-mode of operation) was also tested using an ultralow Ag content to assess its suitability for
101 such applications. On the whole, these high-performance and inexpensive catalysts with ultralow noble

metal content could provide the basis for the development of advanced materials for the DLT oxidation of VOCs.

2. Materials and Methods

2.1. Chemicals and materials

Potassium permanganate ($KMnO_4$; ⩾ 99%), manganese(II) acetate (MnAc ($C_4H_6MnO_4$); 98%), Ag nitrate ($AgNO_3$; ⩾ 99%), quartz sand (SiO_2), and paraformaldehyde (pFA ($HO(CH_2O)_nH$); 95%) were procured from Sigma-Aldrich (St. Louis, Missouri, United States of America (USA)). Commercial $CaCO_3$ (> 98%) was supplied by Showa Co., Ltd. (Tokyo, Japan). Air (99.999% (21% oxygen (O_2) in nitrogen (N_2) balance)), N_2 (99.999%), and hydrogen (H_2; 99.999%) cylinders were purchased from Union Gas Co., Ltd. (Yongin, Republic of Korea). All the chemicals were used as received without any additional purification. Chicken eggs, supplied by the Korea egg distribution association (Seoul, Republic of Korea), were purchased from a local market. Tap water was used to hard-boil the eggs. The eggshells were then peeled off and thoroughly washed with deionized (DI) H_2O to remove surface impurities. Subsequently, the eggshells were dried at 50°C for 12 h in a convection oven (ED-CO150, Han Yang Scientific Equipment Co., Ltd., Seoul, Republic of Korea). The dried eggshells were then ground (< 1.18 mm) for preparing the catalysts.

2.2. Synthesis of catalysts

The Ag/Eggshell catalyst (Ag content fixed at 0.03 wt.%) was prepared using the standard incipient wetness impregnation (IMP) approach [27]. Eggshell (or $CaCO_3$; 20 g) and $AgNO_3$ (suitable amounts

123 based on the desired metal loading) were added to 100 mL DI H_2O contained in a glass beaker (500
124 mL). The suspension was stirred (500 rpm) for 24 h at room temperature (RT). The glass beaker was
125 then transferred to a convection oven operating at 85°C (12 h) to evaporate the excess solvent and dry
126 the solid. The dried powder was then calcined at 450°C for 3 h in a muffle furnace (MF-05, Han Yang
127 Scientific Equipment Co., Ltd., Seoul, Republic of Korea) under a static air condition to obtain the
128 final catalyst.

129 The Ag-(0.5-5%)-MnO_2/Eggshell composites were synthesized by modifying a protocol reported
130 earlier [28]. Briefly, Ag/Eggshell (or Ag/$CaCO_3$; 1 g) and MnAc (suitable amount per Equation 1)
131 were added to DI H_2O (20 mL) contained in a glass beaker (50 mL). The solution was stirred (500
132 rpm) for 2 h (RT). Subsequently, $KMnO_4$ (suitable amount as per Equation 1) was added to the solution
133 under continuous stirring. The stirring was maintained for another 1 h (RT). The solution was allowed
134 to stand for 2 h at RT. At last, the solution was transferred to the convection oven operating at 85°C
135 for 12 h to obtain the dry catalyst powder. Pristine MnO_2 was also synthesized by following the
136 procedure mentioned above without the addition of Ag/Eggshell. The physicochemical properties of
137 eggshell, $CaCO_3$, and the synthesized catalysts (Ag/Eggshell and Ag-MnO_2/Eggshell) were
138 characterized as described in the supplementary information (SI).

139 $$3\ MnAc + 2\ KMnO_4 + 2\ H_2O \rightarrow 5\ MnO_2 + 2\ CH_3COOK + 4\ CH_3COOH \quad (1)$$

140

141 *2.3. Catalysis experiments*

142 The FA oxidation experiments were conducted at atmospheric pressure using a fixed bed quartz
143 reactor (inner radius and length of 2 and 110 mm, respectively). For each experiment, a physical
144 mixture of the catalyst (30-120 mg) and SiO_2 (600 mg) was filled into the reactor and sandwiched

between quartz wool end plugs (Ohio Valley Specialty Company, Marietta, Ohio, USA). Note that the physical mixing of the catalyst with SiO_2 is a routine protocol to avoid flow channeling and localized heating of the packed bed [29, 30]. The reactor temperature was controlled using an electric heater (TC200P (K), Misung Scientific Co., Ltd., Yangju, Republic of Korea). Before each experiment, the catalyst bed was conditioned at 300°C for 3 h under the flow (50 mL min^{-1}) of (i) N_2 or (ii) an H_2 (10%) + N_2 mixture. In the latter case, i.e., the H_2 + N_2 mixture, the designation 'R' was added after the name of the catalyst to denote the thermal reduction pre-treatment. The gas flow through the fixed bed reactor was maintained using a vacuum pump (DOA-P704-AC, Gast Manufacturing Inc., Fair Plain, Michigan, USA). The exact flow rate was set using a flow control valve and calibrator (FC-M1, Sibata Scientific Technology Ltd., Saitama, Japan).

The standard pFA sublimation protocol was employed to prepare the FA gaseous primary standard (G-PS) [31]. Briefly, pFA (100 mg) was filled in the quartz reactor and heated at 130°C under N_2 flow (100 mL min^{-1}) for 50 min. The FA-rich effluent was collected in a 5-L polyester aluminum (PEA) bag (Top Trading Co., Ltd., Seoul, Republic of Korea). The exact FA concentration in the G-PS was quantified using a standard 2,4-dinitrophenylhydrazine-based high-performance liquid chromatography protocol [31]. FA gaseous working standards (G-WS) in the 35-2,500 ppm range were then prepared by diluting the G-PS with air in a 100 L PEA bag. The RH in the prepared G-WS can be neglected (< 10 ppm). For the experiments carried out in the presence of moisture, 680-2,000 µL of DI H_2O was injected (liquid phase syringe (500 µL), Trajan Scientific and Medical, Ringwood, Australia) into the 100 L FA G-WS bag to obtain the RH in the 30-90% range. The FA G-WS was pulled through the fixed bed reactor in the 50-500 mL min^{-1} flow rate range.

The reactor temperature was raised at intervals of 25°C starting from RT (30°C) up to the point of 100% FA conversion (X_{FA}) (Equation 2). Note that $[FA]_{out}$ and $[FA]_{in}$ indicate the FA concentration

168 at the outlet and inlet of the fixed bed reactor, respectively. The FA G-WS flow at each temperature
169 point was maintained for at least 30 min to establish the steady-state condition. A gas chromatograph
170 (GC) equipped with a flame ionization detector (FID) and methanizer was used to quantify both FA
171 and CO_2, respectively (iGC-7200, DS Science Inc., Gwangju, Republic of Korea). The GC oven,
172 methanizer, and FID temperatures were maintained at 150, 320, and 280°C, respectively. The GC
173 analysis time and sample injections were set to 2.5 min and 500 µL, respectively (gastight syringe (500
174 µL), Trajan Scientific and Medical, Ringwood, Australia).

175 The CO_2 yield (Y_{CO2}) was computed using Equation 3 [13]. Note that $[CO_2]_t$ indicates the
176 theoretical amount of CO_2 that should be produced at complete FA mineralization (in terms of the
177 carbon mass balance). In contrast, $[CO_2]_e$ indicates the amount of CO_2 detected experimentally at the
178 outlet of the fixed bed reactor. The steady-state FA reaction rate (r, mmol g^{-1} h^{-1}) was computed using
179 Equation 4 [26, 32, 33]. Note that V_{FA} indicates the FA G-WS flow rate (mol s^{-1}). *In-situ* DRIFTS was
180 conducted using a Tensor II spectrometer (Bruker Corp., Billerica, Massachusetts, USA) equipped
181 with an *in-situ* diffuse-reflectance cell (Harrick Scientific Products, Inc., Pleasantville, New York,
182 USA) [34]. The *in-situ* DRIFTS spectra were acquired at 100°C (in the dark) for two gaseous streams:
183 (i) FA + O_2 (1:1 mixture) and (ii) FA + helium (He; 1:1 mixture).

184 $$X_{FA}(\%) = \left(\frac{[FA]_{in} - [FA]_{out}}{[FA]_{in}}\right) \times 100 \quad (2)$$

185 $$Y_{CO_2}(\%) = \left(\frac{[CO_2]_e}{[CO_2]_t}\right) \times 100 \quad (3)$$

186 $$r = \left(\frac{3{,}600 \times 10^6 \times X_{FA} \times V_{FA}}{m_{cat}}\right) \quad (4)$$

187

188 *2.4. DFT model and method*

189 The mechanism and energetics of the oxidation of FA on the catalytic substrates tested in this
190 study were assessed using DFT calculations. A Spanish Initiative for Electronic Simulations with
191 Thousands of Atoms (SIESTA) model built on pseudopotential codes was utilized for the
192 theoretical calculations [35]. All the calculations were conducted using the Perdew-Burke-
193 Ernzerhof generalized gradient approximation (GGA-PBE) with spin-polarization and van der
194 Waals (+*vdW*) corrections for accurate descriptions of the weak non-covalent interactions [36, 37].
195 Relevant theoretical codes were employed to optimize the atomic positions in the simulated models.
196 During optimizations, the ion cores were described by non-relativistic and norm-conserving
197 pseudopotentials with cut-off radii of Ag, manganese (Mn), oxygen, calcium, nitrogen, and
198 hydrogen as 2.21, 2.26, 1.15, 1.14, 2, and 1.25 au, respectively [38]. Moreover, the wave functions
199 for all species were expanded with a double-ζ plus polarization basis of localized orbitals
200 (excluding hydrogen). A double-ζ basis was applied for hydrogen.

201

202 **3. Results and discussion**

203 *3.1. Characterization of the test materials*

204 *3.1.1. Physical characteristics*

205 The physical characteristics of $CaCO_3$, eggshell, and Ag-MnO_2/Eggshell composites were
206 analyzed using scanning electron microscope (SEM) images, transmission electron microscope
207 (TEM) images, Ag particle size distribution analysis, powder X-ray diffraction (PXRD) patterns,
208 thermogravimetric analysis (TGA), N_2 adsorption-desorption isotherms, pore size distribution
209 analysis, and inductively coupled plasma optical emission spectrometry (ICP-OES). The SEM
210 images of eggshell and $CaCO_3$ showed staggered structures with jagged morphologies in line with

previous observations [22, 23] (Figures S1 (a) and (b)). The presence of tiny pores on the surface of Ag-MnO_2/Eggshell composites may reflect the liberation of organic matter during the calcination process used during synthesis [39] (Figures S1 (c) and (g)). The surfaces of Ag-MnO_2/Eggshell/$CaCO_3$ composites were also covered with MnO_2 flakes (Figures S1 (d) and (h)).

The TEM image revealed a nano rod-like morphology of MnO_2, as reported previously [40, 41] (Figure S2 (a)). The (101) MnO_2 crystal facet (0.405 nm interplanar spacing) was observed in the magnified TEM image [41] (Figure S2 (b)). TEM images of both Ag- and Ag-1.5%-MnO_2/Eggshell confirmed the presence of Ag (111) particles (interplanar distance of 0.232 nm) in both catalysts [42] (Figures S3 (a) and (b)). The average particle sizes of Ag in Ag- and Ag-1.5%-MnO_2/Eggshell were 5.1 ± 1.6 and 4.7 ± 1.6 nm, respectively (Figures S3 (c) and (d)). Accordingly, the particle size of Ag in the Ag-MnO_2 composite seems to be smaller than that of its non-MnO_2 counterpart.

As seen from the PXRD analysis, the characteristic peaks of MnO_2 with the 2θ values of 12.3, 25.1, 37, 41.7, and 65.7° were observed consistently with the (001), (002), (100), (-112), and (110) lattice planes of the layered birnessite (MnO_2) structure, respectively [15, 43] (Figure S4). The PXRD patterns of $CaCO_3$, eggshell, and Ag-MnO_2/Eggshell samples matched well with that simulated for calcite (Figure 1 (a)). The characteristic PXRD peaks at 23.1, 29.4, 31.8, 36.1, 39.6, 43.1, 47.3, 47.6, 48.6, 56.8, 57.5, 60.1, and 64.9° were attributed to the (012), (104), (006), (110), (113), (202), (024), (018), (116), (211), (122), (214), and (300) calcite lattice planes, respectively [44] (Figure 1 (a)). For Ag/Eggshell, a characteristic Ag (111) peak was observed at 38.3°, while a minor Ag (200) peak was present at 44.6° [42] (Figure 1 (a)). The absence of MnO_2 peaks in the PXRD patterns of Ag-MnO_2/Eggshell indicate the high dispersion of MnO_2 in the composites [45, 46]. It can be inferred that MnO_2 loading does not alter the inherent crystal structure of the

composite materials. Furthermore, there were no apparent distinctions in PXRD patterns between the reduced (e.g., Ag/Eggshell-R and Ag-1.5%-MnO_2/Eggshell-R) and non-reduced samples. As such, the reduction pre-treatment does not affect the inherent crystal structure of the catalysts (Figure S5).

Based on the TGA, eggshell displayed three distinct mass loss regions as follows: (i) removal of physisorbed moisture and organic matter (RT-630°C), (ii) decomposition and conversion of the calcite structure to calcium oxide (CaO) with CO_2 liberation (630-777°C), and (iii) structural decomposition (> 777°C) [47] (Figure 1 (b)). In line with our general expectations, $CaCO_3$ did not undergo any significant mass loss events (e.g., up to 604°C) as it does not contain any organic matter in its structure (unlike eggshell) (Figure 1 (b)). Ag/Eggshell closely traced the $CaCO_3$ TGA profile since most of the organic matter contained in its structure must have been released during the calcination step employed in its synthesis [39] (Figure 1 (b)). The Ag-MnO_2 composites displayed an additional mass-loss event between 376-620°C due to the liberation of MnO_2 lattice oxygen (O_{latt}) and phase transformation to other manganese oxide (MnO_x) species [48, 49] (Figure 1 (b)). The TGA profiles of the Ag-MnO_2 composite are likely to involve the desorption of MnO_2 surface active oxygen (O*) species (RT-376°C) and MnO_x phase transformations (> 376°C) [40, 48, 49] (Figure 1 (b)). These additional mass loss events should have lowered the overall thermal stability of Ag-MnO_2 composites (e.g., compared to $CaCO_3$, eggshell, and Ag/Eggshell) (Figure 1 (b)).

The N_2 adsorption-desorption isotherms for all the tested materials displayed a type-IVa pattern typical of mesoporous materials [50] (Figure 1 (c)). The low P/P_0 region in the N_2 adsorption-desorption isotherm indicates the complete filling of micropores by N_2 molecules. The moderate and high P/P_0 regions in the N_2 adsorption-desorption isotherm indicate the mono- and

multilayered N_2 adsorption processes. The presence of a hysteresis loop at elevated P/P_0 (close to unity) is indicative of N_2 adsorption into the mesopores *via* capillary condensation [51] (Figure 1 (c)). The H3-type hysteresis loop indicates the presence of non-rigid plate-like aggregated particles [50] (Figure 1 (c)). The pore size distribution analysis further confirmed that all the analyzed materials contain both micro- (0.8-2 nm pore diameter) and mesopores (2-18 nm pore diameter) in their structures (Figure 1 (d)). The Brunauer-Emmett-Teller (BET) surface area, pore volume, and Barrett-Joyner-Halenda (BJH) average pore diameter values for all the analyzed materials are summarized in Table S1. The actual contents of Ag and Mn in the catalyst samples were quantified using ICP-OES as listed in Table S1. There was good compatibility in the amounts of Ag and Mn between the theoretical and experimental values. Furthermore, the Ag content remained the same for the MnO_2-loaded Ag/Eggshell catalysts to rule out any Ag leaching during the synthesis procedure (Table S1).

3.1.2. Surface Chemistry

The energy-dispersive X-ray spectroscopy (EDX) mapping was utilized to analyze the elemental distribution on the eggshell, $CaCO_3$, and catalyst surfaces (Figure S6). In line with general expectation, calcium, oxygen, and carbon were dominant species on the surfaces of all the analyzed materials (Figure S6). Interestingly, nitrogen was observed to be present on the eggshell surface, while it was absent on the $CaCO_3$ surface. This observation confirmed the presence of protein membranes in the former (Figures S6 (a) and (b)). The observed nitrogen on all the catalyst surfaces (including Ag-1.5%-MnO_2/$CaCO_3$) seems to originate from the protein membranes in the eggshell and the nitrogen in $AgNO_3$ (Figures S6 (c)-(h)). Fluorine impurities were also present on the surfaces of all the eggshell-based materials (Figure S6). It was reported that the fluorine

(present in potable H_2O and the feed components) consumed by laying hens often ends up in the eggshell during its mineralization [52]. In addition, the presence of Ag and Mn on the Ag-MnO_2 catalyst surfaces indicates the successful formation of the catalytic materials (Figure S6). The surface Ag content for all the catalysts was estimated as ~ 1% by the EDX (Figure S6). The low surface area of the eggshell (or $CaCO_3$) support likely concentrates the Ag species on the surface to increase their surface concentrations (compared to the bulk Ag loading).

The Fourier-transform infrared spectroscopy (FTIR) was utilized to assess the functionalities present on the eggshell, $CaCO_3$, and catalyst surfaces (Figure S7). The similar FTIR spectra for all the analyzed materials indicate that Ag and MnO_2 loading onto the $CaCO_3$/eggshell support does not alter the inherent surface functional groups (Figure S7). Also, the reduction pre-treatment did not affect the inherent surface functionalities as both Ag/Eggshell-R and Ag-1.5%-MnO_2/Eggshell-R displayed FTIR spectra similar to their non-reduced counterparts (Figure S7). The characteristic band at 712 cm^{-1} was ascribed to the Ca-O bond [53] (Figure S7). The well-defined bands at 882 and 1401 cm^{-1} were attributed to the carbonate (CO_3^{2-}) bending modes and C-O stretching, respectively [54] (Figure S7). The weak band at 1785 cm^{-1} was ascribed to the CO_3^{2-} C=O bond [13] (Figure S7).

X-ray photoelectron spectroscopy (XPS) was utilized to assess the electronic states of the elements present on the $CaCO_3$, eggshell, and catalyst surfaces. The deconvoluted core level Ca 2p $CaCO_3$ spectrum revealed the presence of the characteristic spin-orbit doublet peaks at 346.6 ($2p_{3/2}$) and 350.1 eV ($2p_{1/2}$) [55] (Figure S8 (a)). The characteristic $CaCO_3$ energy loss satellite features were consistently observed for all the analyzed materials at higher binding energies (BEs; 354.6-358.8 eV) [55, 56] (Figure S8). The presence of a blue-shift (increase in BE: +0.1 eV) in eggshell Ca $2p_{3/2}$, which was absent from $CaCO_3$, may reflect the possible presence of protein

303 membranes in its structure (Figure S8 (b)). The Ca $2p_{3/2}$ peaks for Ag- and Ag-MnO_2/Eggshell
304 catalysts also displayed blue-shifts (compared to eggshell) in the +0.1 to +0.3 eV range, indicating
305 further alterations in the electronic environment of the eggshell support due to Ag and MnO_2
306 loading (Figures S8 (c)-(g)).

307 As compared to $CaCO_3$, the Ca $2p_{3/2}$ and $2p_{1/2}$ peaks of Ag-1.5%-MnO_2/$CaCO_3$ displayed blue-
308 shifts of +0.4 and +0.3 eV, respectively. These findings also support the strong interactions
309 between the loaded Ag and MnO_2 species and the CO_3^{2-} support material (Figure S8 (h)). As
310 compared to Ag/Eggshell, the Ca $2p_{3/2}$ and $2p_{1/2}$ peaks of Ag/Eggshell-R displayed blue-shifts of
311 +0.3 each to reflect the alterations in the local electronic environment by the reduction pre-
312 treatment (Figure S8 (i)). In contrast, the Ag-1.5%-MnO_2/Eggshell-R Ca $2p_{3/2}$ peak underwent a
313 red-shift (lowering of BE) of -0.1 eV (compared to its non-reduced counterpart) to signify slight
314 variations in the local electronic environment, possibly due to hydrogen adsorption onto the MnO_2
315 co-catalyst (see Section 3.3.2) (Figure S8 (j)).

316 The deconvoluted core level C 1s $CaCO_3$ spectrum displayed a characteristic CO_3^{2-} peak at
317 289.1 eV [56] (Figure S9 (a)). The additional peaks at 284.6, 286.3, and 287.7 eV were attributed
318 to the C-C, C-O, and O-C-O functionalities of the surface-adsorbed hydrocarbon impurities,
319 respectively [56] (Figure S9 (a)). Similar peaks were also observed in the core level C 1s eggshell
320 spectrum in the 284.7-289.1 eV range (Figure S9 (b)). The peak at 286.1 eV in the C 1s eggshell
321 spectrum was also attributed to the C-N group in the protein membranes alongside the C-O
322 functionality of the surface-adsorbed hydrocarbons (Figure S9 (b)). The Ag/Eggshell CO_3^{2-} peak
323 with a blue-shift of +0.3 eV (compared to eggshell) indicates the possible alterations in the local
324 electronic environment due to Ag loading (Figure S9 (c)). Compared to Ag/Eggshell, the CO_3^{2-}
325 peak in the core level C 1s spectra of Ag-MnO_2/Eggshell catalysts displayed red-shifts in the -0.9

to 0.2 eV range (Figures S9 (d)-(g)). Ag-1.5%-MnO_2/$CaCO_3$ displayed a red-shift of -0.1 eV for the CO_3^{2-} peak compared to $CaCO_3$ (Figure S9 (h)). The CO_3^{2-} peak appeared at 289 eV for both Ag/Eggshell-R (redshift of -0.4 eV compared to the non-reduced counterpart) and Ag-1.5%-MnO_2/Eggshell-R (blue shift of +0.3 eV compared to the non-reduced counterpart) (Figures S9 (i) and (j)). These observations provide evidence for complex interactions between the Ag and MnO_2 species and the eggshell/$CaCO_3$ support (see Section 3.3.2).

The deconvoluted core level O 1s spectrum revealed the presence of CO_3^{2-} O_{latt} (O_I) and C-O/O-C-O species at 531.1 and 533 eV for both $CaCO_3$ and eggshell [56] (Figures S10 (a) and (b)). The Ag/Eggshell O_I peak displayed a blue-shift of +0.2 eV (compared to eggshell) (Figure S11 (a)). The peak at 531.7 eV in the core level O 1s Ag/Eggshell spectrum was attributed to adsorbed oxygen (O_{ads} (O^-, O_2^-, and O_2^{2-})) species (O_{II}) [13] (Figure S11 (a)). A new peak in the 529.3-529.6 eV range was observed in the Ag-MnO_2/Eggshell/$CaCO_3$ core level O 1s spectrum, which was attributed to the MnO_2 Olatt (O_{III}) [57] (Figures S11 (b)-(f)). The relative contribution of the O_{III} peak in the core level O 1s spectrum rose from 8.1 to 37.1%, with a corresponding increase in the MnO_2 loading (0.5-5%) in the Ag-MnO_2 composites (Figures S11 (b)-(f)). The O_I peak displayed red-shifts in the -0.3 to -0.1 eV range for the Ag-1.5-5%-MnO_2/Eggshell catalysts (Figures S11 (c)-(e)). On the other hand, the Ag-1.5%-MnO_2/$CaCO_3$ O_I peak displayed a blue-shift of +0.3 eV (compared to $CaCO_3$), possibly due to alterations in the local electronic environment of the concerned species (Figure S11 (f)). The Ag/Eggshell-R and Ag-1.5%-MnO_2/Eggshell-R O_I peaks appeared at 531.4 eV (blue shift of +0.1 eV compared to the non-reduced counterpart) and 531 eV (redshift of -0.1 eV), respectively (Figures S11 (g) and (h)). The O_{III} Ag-1.5%-MnO_2/Eggshell peak underwent a red-shift of -0.5 eV after the reduction pre-treatment (Figure S11 (h)). The overall results of this comparative analysis suggest that there should have been complex alterations

in the inherent surface chemistry of the eggshell/$CaCO_3$ support due to Ag and MnO_2 loading and the reduction pre-treatment (see Section 3.3.2).

The deconvoluted spectra of Ag 3d core level in Ag/Eggshell revealed characteristic spin-orbit doublet peaks at 368.1 ($3d_{5/2}$) and 374 eV ($3d_{3/2}$), indicating the existence of metallic Ag species (Ag^0) [13] (Figure 2 (a)). The calcination treatment employed for the synthesis of catalyst is likely to decompose the silver oxide (Ag_2O) species to yield Ag^0 [13, 58]. The Ag-MnO_2/Eggshell Ag $3d_{5/2}$ peaks displayed red-shifts of -0.4, -0.5, -0.6, and -0.7 eV (compared to Ag/Eggshell) as the MnO_2 loading increased from 0.5 to 5% (Figures 2 (b)-(e)). The Ag $3d_{5/2}$ and $3d_{3/2}$ Ag-1.5%-MnO_2/$CaCO_3$ peaks both displayed a blue-shift of +0.3 eV compared to the eggshell sample. As such, there should be inherent differences between the eggshell and $CaCO_3$ supports (Figure 2 (f)). Similarly, both the Ag $3d_{5/2}$ and $3d_{3/2}$ Ag/Eggshell-R peaks displayed a blue-shift of +0.3 eV compared their non-reduced counterparts (Figure 2 (g)). In contrast, no changes in the Ag $3d_{5/2}$ peak position were observed for Ag-1.5%-MnO_2/Eggshell-R (compared to its non-reduced counterpart), while the $3d_{3/2}$ peak displayed a red-shift of -0.1 eV (Figure 2 (h)). This indicates the possibility of strong Ag-MnO_2 interactions involving electron transfers at the bimetallic interface and the eggshell support with the reduction pre-treatment for altering the inherent electronic environment of the catalysts [13]. The surface Ag content in the catalysts varied in the 0.16-1.6 atomic (at.)% range as determined by the XPS (Table S1).

The deconvoluted core level Mn 2p spectra revealed the spin-orbit $2p_{3/2}$ and $2p_{1/2}$ splitting characteristic of MnO_2 [59, 60] (Figure 3). The Mn $2p_{3/2}$ peak was deconvoluted into two peaks characteristic of the Mn^{3+} (640.5-642.2 eV) and Mn^{4+} (642.7-644 eV) species [61] (Figure 3). The co-existence of Mn^{4+} and Mn^{3+} species indicates that the electrostatic balance in MnO_2 is maintained through the formation of oxygen vacancies (O_{vac}) [48] (Equation 5). The Ag-MnO_2

372 Mn^{3+} peaks underwent blue-shifts (+0.2-+0.4) when the MnO_2 loading increased from 0.5 to 5%
373 (Figure 3). The Ag-1.5%-MnO_2/Eggshell-R Mn^{3+} and Mn^{4+} peaks displayed red-shifts of -1.5 and
374 -1.2 eV, respectively, compared to its non-reduced counterpart (Figure 3). It was reported that
375 unsaturated Mn^{4+}/Mn^{3+} species around the pores could increase the electron (e^-) density of Mn
376 species to lower BEs in the XPS spectra [61]. The surface Mn content in the catalysts varied in the
377 3.4-14 at.% range as determined by the XPS (Table S1).

378 $4\ Mn^{4+} + O^{2-} \rightarrow ½\ O_2 + 2\ e^-/O_{vac} + 4\ Mn^{4+} \rightarrow O_{vac} + ½\ O_2 + 2\ Mn^{4+} + 2\ Mn^{3+}$ (5)

379 The carbon monoxide (CO)-temperature-programmed desorption (TPD) result (until 383 K) is
380 presented in Figure 4. For higher temperatures, no peaks related to CO desorption were observed.
381 The total signal shows two desorption peaks with parameters $A_1 = (1.35 \pm 0.05)\ 10^{+14}\ s^{-1}$ and $E_1 =$
382 152.6 ± 5.5 kJ mol^{-1} and $A_2 = (1.54 \pm 0.06)\ 10^{+6}\ s^{-1}$ and $E_2 = 79.0 \pm 3.0$ kJ mol^{-1}, respectively (refer
383 to the SI). The above results suggest two possible adsorption sites for CO on the Ag-1.5%-
384 MnO_2/Eggshell-R catalyst. The first peak accounts for 47.8% of the total signal, and the second
385 accounts for 52.2%. Both desorption peaks contribute almost equally to the net signal. For a
386 reaction temperature of 350 K, the desorption coefficients were $2.56\ 10^{-6}$ and $2.36\ 10^{-9}\ s^{-1}$,
387 respectively. As the above-presented values are rather low, further oxidation of CO into CO_2 is
388 most likely.

389 Figure 5 shows a typical output during the H_2-temperature-programmed reduction (TPR)
390 experiment ($\beta = 2$ K min^{-1} (refer to the SI)). A pronounced peak starting at ~800 K was observed,
391 which corresponds to the degradation of the eggshell support. This was also confirmed by the TGA
392 data. The shape of the H_2-TPR data profile corresponds well with that typically reported for $CaCO_3$
393 degradation [62]. The degradation of the eggshell above 800 K was also observed during the CO-

TPD experiment. Therefore, the TPR data to investigate the reduction by H_2 were only considered below 723 K. Figure 6 provides the results for all the tested heating rates with four distinct reduction peaks being observed. The TPR data were modeled using Gaussian peak analysis as described in the SI. The corresponding values for T_{max} (refer to the SI (Section S1)) are reported in Table S2. The regression of data couples (T_{max}, β) according to Equation 8 in SI delivers the activation energy (E_i) and the pre-exponential factor (A_i) per reduction peak (Figure 7 (a)).

The E_i (kJ mol^{-1}) increased in the following order: 106.3 (peak 3) < 130.5 (peak 1) < 146.9 (peak 2) < 170.3 (peak 4). It is striking that the third peak shows low E_i and A_i. Note that it is not mandatory for the E_i values to show an increasing trend with increasing reduction temperatures [63]. E_i between 61 and 149 kJ mol^{-1} have been reported previously for the surface reduction of MnO_x [64]. Previous reports also indicate the O_{vac} formation energies for MnO_2 ranged from 0.7 eV (67.5 kJ mol^{-1}) to 2.45 eV (236.4 kJ mol^{-1}) [65]. Hence, all the obtained E_i in the present work are considered to be physically sound. A previous study also reported two reduction peaks ranging between 500 and 770 K for MnO_x [66]. The reduction of MnO_2 should involve subsequent transitions to Mn(III) oxide (Mn_2O_3) and trimanganese tetraoxide (Mn_3O_4) (Equations 6-7) [66]. As the further reduction of Mn_3O_4 occurs at temperatures greater than 723 K, it was not considered in the present work due to the co-occurrence of the $CaCO_3$ degradation peak [67]:

$$2\ MnO_2 + H_2 \rightarrow Mn_2O_3 + H_2O \quad (6)$$

$$3\ MnO_2 + 2\ H_2 \rightarrow Mn_3O_4 + 2\ H_2O \quad (7)$$

Based on the thermodynamic data reported previously, the entropy (ΔS_{red}) values at 500 K for the bulk reduction reactions (Equations 6-7) were calculated to be -50.1 and -70 J mol^{-1} K^{-1}, respectively [68]. The corresponding enthalpy values were calculated to be -81.4 and -103.4 kJ

mol^{-1}, respectively. Expressing the ΔS_{red} change per removed oxygen atom, we get values of -50.1 and -35.0 J mol^{-1} K^{-1}, respectively.

For an irreversible reaction, the relation between the A_i and $\Delta S^{\neq}$ (the difference between the ΔS_{red} of the activated complex and reactants) can be calculated using Equation 8:

$$A_i = \frac{k_B T}{h} \exp\left(\frac{\Delta S^{\neq}}{R}\right) \quad (8)$$

The importance of $\Delta S^{\neq}$ is that it contributes to the shift in equilibrium between the reactants and activated complexes *via* the usual thermodynamic relationship ($\Delta G^{\neq} = \Delta H^{\neq} - T \cdot \Delta S^{\neq}$). The value for $\Delta H^{\neq}$ can be taken as the E_i (with a maximal deviation of 10%). An increase for $\Delta S^{\neq}$ lowers $\Delta G^{\neq}$, and the corresponding equilibrium shifts towards the formation of the activated complex for the surface reduction reaction [69]. Using the data from Table S2 and Equation 8, the following values were obtained for $\Delta S^{\neq}$ (calculated at T_{max} from the TPR data with β = 10 K min^{-1}): 10.6 ± 3.2, 7.9 ± 0.9, -114.2 ± 24.9, and -47.1 ± 5.4 J mol^{-1} K^{-1}. Results for β = 2 K min^{-1}, differ by less than 3.7%, so the given values were considered acceptable for comparison.

For the first and second reduction peaks, the $\Delta S^{\neq}$ was positive, indicating a shift in the transition state more towards H_2O desorption. The above result indicates a faster reductive desorption process. The fact that the E_i was higher for the second peak (146.9 ± 16.4 kJ mol^{-1}) compared to the first peak (130.5 ± 3.6 kJ mol^{-1}) reflects the local surrounding and possible synergistic effects in the former condition. For the third and fourth peaks, negative $\Delta S^{\neq}$ values were obtained, indicating that the transition state was closer to the surface oxygen. Hence, the third and fourth peaks likely correspond to the bulk reduction reactions (Equations 6-7). Upon comparison of the

436 data, the $\Delta S^{\neq}$ values follow the same trend as the previously mentioned ΔS_{red} difference per oxygen
437 atom in the transition state. A more pronounced value was found for the third peak, but it is
438 compensated for by corresponding lower E_i values of 106.3 ± 12.3 and 170.3 ± 19.5 kJ mol^{-1}. The
439 above values also showed a similar increasing trend with the thermodynamically calculated
440 reaction enthalpies for Equations 6-7.

441 Before each TPR experiment, the sample was flushed with argon (Ar) to remove the weakly
442 adsorbed (physisorbed) oxygen species (refer to the SI). In this respect, the first two peaks were
443 considered to correspond to the reduction of oxygen species on the catalyst surface (O_{II}). It is
444 known that these surface oxygen species have high mobility, and they are easier to remove under
445 reducing conditions (compared to the bulk oxygen diffusion). This is reflected in lower reduction
446 temperatures. Upon analyzing the thermodynamic data, the other two peaks were assigned to the
447 bulk reduction processes (Equations 6-7). With regard to the XPS results, the O_{II} can be considered
448 to be the O* during FA oxidation, which is then replenished by O_2 in the feed. Similarly, the last
449 two peaks can be related to O_{III}. Note that O_{III} is responsible for the total and selective oxidation
450 reactions [70].

451 The reduction rate coefficient can be evaluated at a typical reaction temperature of 110°C to
452 compare all the oxygen species, giving the following values: 4.50 10^{-5}, 2.14 10^{-7}, 3.31 10^{-8}, and
453 2.49 10^{-13} s^{-1}. The first two peaks (particularly the first one) can be related to the active O* species.
454 According to the approximated Redhead analysis (refer to the SI), increasing E_i values were
455 obtained, as reported in Table S2. The above result corresponds to the peak appearance at higher
456 temperatures. The fraction of the peaks in the total TPR signal is given in Figure 7 (b). The average
457 fractions of each peak were 12.8 ±1.9, 48.1 ± 2.9, 26.5 ± 2.6, and 12.6 ± 3.5%. Almost the same

458 distribution was obtained for each of the tested heating rates. In other words, ~ 60% of the total
459 reaction profile (corresponding to reducible oxygen) was estimated to be the surface oxygen, while
460 the remaining 40% was the bulk oxygen.

461

462 *3.2. Evaluation of the FA catalytic oxidation performance*

463 The steady-state performances of all catalysts against FA in air assessed from light-off curves
464 of the catalytic reactions follow the descending order: Ag-1.5%-MnO_2/Eggshell-R > Ag-3%-
465 MnO_2/Eggshell-R > Ag-1.5%-MnO_2/Eggshell > Ag-5%-MnO_2/Eggshell-R > Ag-1.5%-
466 MnO_2/$CaCO_3$-R > MnO_2-R > Ag-0.5%-MnO_2/Eggshell-R > Ag/Eggshell-R (Figure 8 (a)). The
467 temperature for 90% conversion (T_{90}) of 100 ppm FA followed the ascending order: Ag-1.5%-
468 MnO_2/Eggshell-R (77°C) < Ag-3%-MnO_2/Eggshell-R (93°C) < Ag-1.5%-MnO_2/Eggshell (96°C)
469 < Ag-1.5%-MnO_2/$CaCO_3$-R (97°C) < MnO_2-R (99°C) < Ag-5%-MnO_2/Eggshell-R (113°C) < Ag-
470 0.5%-MnO_2/Eggshell-R (123°C) < Ag/Eggshell-R (175°C) (Table 1). The above results indicate
471 that the catalytic activity increases with a rise in MnO_2 loading from 0.5 to 1.5%, although a further
472 increase in the MnO_2 loading lowers the catalytic activity (Figure S12). The latter pattern may
473 reflect the agglomeration of MnO_2 particles, which may cover up the active surface sites to hinder
474 their access to the FA molecules. The r-value (quantified at 80°C) ranged from 2.6 mmol g^{-1} h^{-1}
475 (Ag/Eggshell-R) to 9.4 mmol g^{-1} h^{-1} (Ag-1.5%-MnO_2/Eggshell-R) (Table 1). In line with our
476 general expectation, both X_{FA} and Y_{CO2} increased steadily with temperature (Figures 8 (a) and
477 S13). Both the Y_{CO2} and X_{FA} reached 100% at the same temperature, indicating the complete
478 mineralization of FA into CO_2 (as per the carbon balance) (Figures 8 (a) and S13). Nevertheless,
479 at temperatures less than T_{90}, the Y_{CO2} was often observed to be lower ($\leqslant$ 0.5 times) than the

480 corresponding X_{FA} value for all the tested catalysts, indicating partial mineralization of FA (see
481 Section 3.3) (Figures 8 (a) and S13).

482 At 80°C, the r-value for Ag-1.5%-MnO_2/Eggshell-R was about 3.7 times larger than that of
483 Ag/Eggshell-R (Table 1). Clearly, the synergy of Ag-MnO_2 appears to enhance the activity of the
484 supported Ag catalyst for the FA oxidation reaction. Likewise, the synergistic effect between noble
485 metal and MnO_2 was reported to boost the FA oxidation reaction [18, 71]. Furthermore, the
486 observations of 24% higher performance of Ag-1.5%-MnO_2/Eggshell-R (in terms of the r-value at
487 80°C relative to its non-reduced counterpart) confirm the net catalytic activity enhancement due
488 to reduction pre-treatment (Table 1).

489 Interestingly, the performance of Ag-1.5%-MnO_2/Eggshell-R was also seen to be better by 40%
490 than the corresponding catalyst made of the pure $CaCO_3$. This difference indicates the superiority
491 of the eggshell support over its commercial counterpart (Table 1). A similar result was also
492 reported earlier wherein the thermocatalytic oxidation of gaseous benzene was compared between
493 Ag/Eggshell and Ag/$CaCO_3$ [13]. Our previous study on the application of the K-Pt/Eggshell
494 catalysts for FA oxidation also demonstrated the superior activity of the eggshell-based catalyst
495 over the one synthesized using the commercial $CaCO_3$ support [26]. The superior performance of
496 eggshell over $CaCO_3$ can be primarily attributed to the presence of surface defects in the former,
497 as they may act as the primary sites for FA adsorption and subsequent activation [22, 26]. The
498 larger surface area of Ag-1.5%-MnO_2/Eggshell over its $CaCO_3$ counterpart (e.g., by 1.8 times)
499 also supports the above hypothesis (Table S1). The surface-bound organic matter (e.g., protein) in
500 the eggshell could be liberated during the calcination step to yield a higher surface area than the
501 $CaCO_3$ counterpart [26, 39]. In line with the above discussion, it has been previously reported that
502 such pores and defects often determine the overall catalytic activity [22, 72]. The best-performing

503 catalyst (Ag-1.5%-MnO_2/Eggshell-R) was utilized for further experiments to evaluate the effect
504 of process variables on FA oxidation.

505 The decrease in X_{FA} at 80°C with a decrease in m_{cat} was observed in the following order: 120
506 mg (92%) > 60 mg (82%) > 30 mg (62%) (Figure 8 (b)). The decrease in X_{FA} at smaller m_{cat} is
507 expected due to the decline in the number of available active surface sites to bring about the FA
508 oxidation reaction. An increase in the flow rate from 50 mL min^{-1} (5,308 h^{-1} in terms of gas hourly
509 space velocity (GHSV)) to 500 mL min^{-1} (53,080 h^{-1} GHSV) also lowered the FA removal as
510 reflected by the X_{FA} values (determined at 80°C): 50 mL min^{-1} (92%) > 250 mL min^{-1} (64%) >
511 500 mL min^{-1} (53%) (Figure 8 (c)). We thus inferred that the residence time of the FA molecules
512 inside the reactor is greatly decreased (shortened FA-catalyst contact time) at elevated flow rates,
513 which decreases the overall X_{FA} [73].

514 An increase in the FA concentration resulted in a dramatic decrease in X_{FA} (determined at 80°C):
515 35 ppm (100%) > 100 ppm (92%) > 1,000 ppm (46%) > 2,500 ppm (19%) (Figure 8 (d)). At a
516 given temperature, increases in FA concentrations would saturate the active surface sites to lower
517 the X_{FA} [73]. An increase in the RH level also lowered the X_{FA} (determined at 80°C): ~ 0% RH
518 (92%) > 30% RH (57%) > 60% RH (51%) > 90% RH (49%) (Figure 8 (e)). The decrease in X_{FA}
519 with increasing RH was expected as both FA and H_2O molecules can compete to adsorb on the
520 same active surface sites [73]. The durability and stability of Ag-1.5%-MnO_2/Eggshell-R catalyst
521 were also assessed in the oxidative removal of FA in air at 100°C (Figure 8 (f)). As shown in
522 Figure 8 (f), 100% X_{FA} to CO_2 was stably maintained for the maximum test duration of 50 h TOS
523 without any deactivation.

524 FA oxidation performances between eggshell and $CaCO_3$ were markedly different despite
525 identical crystal structures, as described above. It was observed that the adsorption of FA

molecules onto the support surface is largely controlled by the defects rather than the local chemical composition (see Section 3.3.2). Hence, eggshells with natural cavities should offer a more favorable FA oxidation pathway, as described in earlier work [26]. The presence of abundant surface defects and cavities in eggshells can also be inferred from the fact that the BET surface area of Ag-1.5%-MnO_2/Eggshell is 77% larger than Ag-1.5%-MnO_2/$CaCO_3$ (Table S1). The calcination step (at 450°C) employed in the catalyst synthesis stage should have removed the surface-capped organic matter from the eggshell (absent in $CaCO_3$) to create several defects and cavities (increased specific surface), as also confirmed by the TGA data (Figure 1 (b)).

3.3. FA oxidation pathway and mechanism

3.3.1. In-situ DRIFTS and physicochemical characterization

To estimate the oxidation pathway of FA, the *in-situ* DRIFTS measurements were carried out for both Ag/Eggshell-R (Figures 9 (a) and S14 (a)) and Ag-1.5%-MnO_2/Eggshell-R (Figures 9 (b) and S14 (b)). The following species were identified on the catalyst surfaces during the FA oxidation reaction in the presence of O_2: (i) molecularly adsorbed FA (FA_{ads} (1792 and 1794 cm^{-1})), (ii) formate ($HCOO^-$ (υ(CH) (2851, 2878, 2893, 2988, and 2997 cm^{-1}))) and symmetric/asymmetric OCO vibrational modes (υ_s(OCO)/υ_{as}(OCO)) of monodentate $HCOO^-$ (1350 and 1628 cm^{-1}), (iii) (bi)carbonate (CO_3 (symmetric/asymmetric stretching vibrational mode ($\upsilon_s(CO_3)/\upsilon_{as}(CO_3)$) (1300/1344-1541/1579 cm^{-1}))), (iv) surface hydroxyl (OH (3304/3367-3683/3690 cm^{-1})), (v) CO (2017, 2022, 2028, 2031, 2173, and 2183 cm^{-1}), and (vi) CO_2 (2340, 2341, 2360, and 2371 cm^{-1}) [10] (Figures 9 (a) and (b)).

Based on these observations, it can be inferred that the FA molecules first adsorb on the active surface sites (defects (see Section 3.3.2)) to react with O* for the formation of CO_2 as the end-product *via* $HCOO^-$, CO_3, and CO intermediates [16]. The O* contributes to the formation of formic acid (HCOOH) through combination with FA_{ads}. The HCOOH molecules then decomposed to yield proton (H*) and $HCOO^-$. CO_3 species are then produced through a combination of O* and $HCOO^-$. The CO_3 species then combine with H* to decompose into adsorbed H_2O (H_2O_{ads}) and CO_2 molecules. As CO was found to be one of the reaction intermediates, the $HCOO^-$ species should likely have decomposed into H_2O_{ads} and CO molecules as well. The reaction between CO and O* would then yield CO_2 as the end-product [74]. The consumption of O* (to drive the FA oxidation reaction) forms O_{vac}, which are then replenished through dissociative O_2 adsorption (on Ag nanoparticles (NPs) and MnO_2) to sustain the catalytic pathway.

For the MnO_2 sites, Mn^{3+} is oxidized into Mn^{4+} after O_2 is captured by O_{vac} (formation of O_{ads} species). The e^- released by the Mn^{3+} oxidation process then leads to the conversion of O_{ads} into O* for the oxidation of FA_{ads}. This e^- is also involved in the reduction of the Mn^{4+} species back into Mn^{3+}. Hence, the Mn^{3+}-Mn^{4+} redox cycle sustains the FA oxidation reaction on the MnO_2 sites [16]. The presence of MnO_2 alongside Ag NPs is not likely to alter the FA oxidation pathway significantly as the same reaction intermediates were observed in the *in-situ* DRIFTS spectra of both Ag/Eggshell-R and Ag-1.5%-MnO_2/Eggshell-R (Figures 9 (a) and (b)). Nevertheless, the distinct absence of monodentate $HCOO^-$ in the *in-situ* DRIFTS spectrum of Ag-1.5%-MnO_2/Eggshell-R (compared to Ag/Eggshell-R) indicates slight differences in the nature of FA oxidation products between the Ag- and Ag-MnO_2 catalysts (Figures 9 (a) and (b)). (The presence of bimetallic sites (Ag-MnO_2 interface) could favor the formation of bridging $HCOO^-$ instead.)

The presence of negative surface OH bands in the *in-situ* DRIFTS spectra indicates their consumption during the FA oxidation reaction (Figures 9 (a) and (b)). The surface OH groups have been reported to bring about the direct oxidation of $HCOO^-$ into CO_2 and H_2O_{ads} [75] (Equation 9). The consumed surface OH groups can then be replenished through the combination of O* and H_2O_{ads} to sustain the catalytic pathway [61]. The absence of distinct H_2O_{ads} bands in the *in-situ* DRIFTS spectra further indicated the rapid H_2O_{ads} conversion into surface OH [75] (Figures 9 (a) and (b)). It is likely than only the H_2O_{ads} produced through FA_{ads} conversion produce OH groups, while the H_2O supplied through the moisture in G-WS lowers the catalytic activity (see Section 3.2). The prominence of negative surface OH bonds in the Ag/Eggshell-R *in-situ* DRIFTS spectrum (compared to Ag-1.5%-MnO_2/Eggshell-R) may suggest the more significant contribution of OH induced direct $HCOO^-$ oxidation on the Ag- catalyst surface (Figures 9 (a) and (b)).

$$OH + HCOO^- \rightarrow H_2O_{ads} + CO_2 \quad (9)$$

Most of the above-described reaction intermediates are also observed in the *in-situ* DRIFTS spectra obtained in the He environment. Consequently, we concluded that the surface O_{latt} in the catalyst samples should exist as O* (strong Ag-Eggshell and Ag-MnO_2-Eggshell interactions) to bring about FA oxidation (Figures S14 (a) and (b)). Nevertheless, the FA oxidation reaction cannot be sustained for prolonged periods in an O_2 deficient environment as O_{vac} created by O* consumption cannot be replenished. Interestingly, the surface OH bands in the *in-situ* DRIFTS spectra became more negative during the FA oxidation reaction in the He environment (Figures S14 (a) and (b)). As such, the overall FA oxidation reaction as described in Equation 9 becomes more prominent in the absence of O_2 for both Ag/Eggshell-R and Ag-1.5%-MnO_2/Eggshell-R.

The PXRD pattern of Ag-1.5%-MnO_2/Eggshell-R was not altered after the FA oxidation reaction. This observation is likely to indicate the structural stability of this catalyst (Figures 1 (a) and S15 (a)). Likewise, as there was no change in the Ag-1.5%-MnO_2/Eggshell-R FTIR spectrum after the FA oxidation reaction, the surface functionalities of the catalyst should also be unaffected by such a process (Figures S7 and S15 (b)). The above observations further confirm the complete oxidation of FA_{ads} into CO_2 to match the Y_{CO2} results (see Section 3.2). Similar to the above observations, no new species were identified in the deconvoluted spectra of Ag-1.5%-MnO_2/Eggshell-R XPS after the FA oxidation reaction (Figures S16 and S17). The fact that no changes in the Ca $2p_{3/2}$, Ca $2p_{1/2}$, and CO_3^{2-} (C 1s) peak positions after the FA oxidation reaction further confirms the structural stability of the catalyst (Figures S8 (j), S9 (j), S16 (a), and S16 (b)).

There was no alteration of O_I peak position in the core level O 1s Ag-1.5%-MnO_2/Eggshell-R XPS spectrum after the FA oxidation reaction (Figures S11 (h) and S16 (c)). The O_{II} peak displayed a red-shift of -0.3 eV (Figures S11 (h) and S16 (c)). In comparison, the blue-shift (+0.3 eV) of the O_{III} peak (after the FA oxidation reaction) indicates the alterations in the local electronic environment (Figures S11 (h) and S16 (c)). Also, the relative contributions of the O_I/O_{III} species towards the net O 1s spectrum decreased from 65.3/12.4% to 41.4/9.4% after the FA oxidation reaction (Figures S11 (h) and S16 (c)). In contrast, the relative contribution of O_{II} species increased from 22.3 to 49.2% (Figures S11 (h) and S16 (c)). The enhanced contribution of O_{II} species in the overall O 1s spectrum can be explained by the dissociative O_2 adsorption (O_{ads}) and its subsequent deposition on the catalyst surface during the FA oxidation reaction.

The Ag $3d_{5/2}$ peak also did not show any changes in its position, whereas the Ag $3d_{3/2}$ peak displayed a blue-shift of +0.1 eV. The latter may be accounted for by the differential charging effect (Ag-eggshell interaction) [13] (Figures 2 (h) and S16 (d)). The blue-shifts of +0.7 and +0.6

614 eV (core level Mn 2p spectrum) observed in Mn^{3+} and Mn^{4+} species, respectively, may indicate e^-
615 deficient conditions after the FA oxidation reaction (Figures 3 and S17). A possible explanation
616 for this observation could be the surplus deposition of O_{ads} onto the catalyst surface during the FA
617 oxidation reaction (Mn^{3+} supplies e^- to O_{ads} to yield O*) as also confirmed by the increase in the
618 amount of O_{II} species [16].

619

620 *3.3.2. DFT simulations*

621 A set of first-principle calculations were performed to reveal the X_{FA} steps on diverse eggshell
622 substrates (modified and pristine forms). The eggshell surface was modeled using the (001) surface
623 of $CaCO_3$ [26] (Figure 10 (a)). Dangling bonds present on the $CaCO_3$ surface may have a similar
624 effect as the defects and impurities in eggshells [26]. The dangling bonds were assumed to be
625 present on the carbon atoms. Further, the reduced eggshell was also modeled by assuming that the
626 dangling bonds were saturated with atomic hydrogen (Figure 10 (b)). Catalytic X_{FA} on the pristine
627 eggshell surface was studied as the first step of the theoretical modeling. The physisorption of FA
628 over the natural cavities in eggshells was taken as the preliminary step of the FA-substrate
629 interaction. The FA physisorption step was energetically favorable (adsorption energy of ~ -0.8
630 eV mol^{-1}) for all the tested substrates. The co-adsorption of O_2 does not significantly alter the FA
631 adsorption energy (Figure 10 (b)). Consequently, the physisorption of FA molecules is tightly
632 controlled by the defects and cavities on the $CaCO_3$ surface instead of the local chemical species.

633 In the second step of the theoretical modeling, the solutions for the minimal formation energies
634 (for each reaction step) were derived by considering the energetics of several realistic intermediate

steps in the X_{FA} pathway. The theoretical results suggest that the catalytic X_{FA} proceeds *via* a four-step process (Equations 10-13).

$$H_2CO + A\text{-}O\text{-}A' \rightarrow A'HCOO + AH \quad (10)$$

$$A'HCOO + A\text{-}H \rightarrow CO + A'OH + AH \quad (11)$$

$$A'OH + AH + CO \rightarrow A'OHCO + AH \quad (12)$$

$$A'HCOO + AH \rightarrow CO_2 + A'H + AH \quad (13)$$

Note that A-O-A' is the local chemical environment of the FA_{ads} on the eggshell surface. The reduction pre-treatment converts both A' and A to A'H and AH. The first step of the FA oxidation process involves the breakage of the A-A' oxygen bridge to generate two dangling bonds (A'-O* and A-*). The decomposition of FA_{ads} leads to the saturation of the dangling bonds (A'-O* group interacts with HCO to yield A'HCOO, while the hydrogen atom adsorbs onto A-*). The formed $HCOO^-$ species then decompose to form CO (Equation 11). The formation of $HCOO^-$ and CO as reaction intermediates during FA oxidation has been experimentally confirmed and described in several recent studies (see Section 3.3.1) [10, 26, 76].

In the third and fourth steps of the FA oxidation process, the CO molecules are converted into HO-C*=O intermediate to yield CO_2, which then desorbs from the substrate. The fourth step reduces the eggshell through an AH + A'H mediated substitution of the A-O-A' oxygen bridge. The proposed DFT simulation of the FA oxidation process agrees with the experimentally observed formation of FA oxidation intermediates even in the absence of O_2 (see Section 3.3.1). Alteration of the catalytic substrate during the FA oxidation reaction in the absence of O_2 makes the reaction unsustainable as the depleted O* reserve cannot be replenished. The DFT calculations further indicate that the X_{FA} process is not directly influenced by the co-presence of O_2, and the

differences in the formation energies between the products and intermediates were estimated to be in the range of 0.15 eV mol^{-1}. The O_2 helps sustain the FA oxidation reaction by replenishing the O* stock (recharge of the reduced catalyst) (Equations 14-15).

$$A'H + AH + O_2 \rightarrow AH\text{-}O\text{-}O\text{-}A'H \quad (14)$$

$$A'H + AH + O_2 \rightarrow H_2O + A\text{-}O\text{-}A' \quad (15)$$

In the next step of the DFT simulation, we considered the influence of the modified eggshell surface on the energetics of the FA oxidation reaction. The formation energy for each of the above-described reaction steps was negative (exothermic) for the pristine (001) eggshell surface. It should be noted that the magnitudes of formation energy are relatively small if estimated for the second and third FA oxidation steps on the eggshell surface. Also, the reduction pre-treatment made the FA oxidation process energetically unfavorable on the eggshell surface (Figure 11). Hence, the combined role of surface defects and impurities is expected to play a critical role in the FA oxidation reaction over eggshells. The last step of the FA oxidation reaction, i.e., the desorption of CO_2, requires ~ 30 kJ mol^{-1} for all the substrates considered in this study.

The effect of MnO_2 co-catalyst and Ag-doping on the FA oxidation reaction was further studied using DFT simulations. First, the locations of Ag impurities on the eggshell surface were determined. According to the simulation results, the formation energy of interstitial Ag is ~ -2 eV $atom^{-1}$ in contrast to the positive formation energy for the substitutional impurity cases (Figures 10 (a) and (b)). The theoretical simulation result agrees with the experimentally determined Ag 3d XPS spectra (see Section 3.1.2). A MnO_2 slab was utilized to conduct DFT simulations in line with the experimentally measured Mn 2p XPS spectra (see Section 3.1.2) (Figure 10 (c)).

678 The formation of Ag-oxygen bonds could result in the possible substitution of C-A to C-Ag, as
679 expressed in Equations 10-13. The presence of Ag species (metallic or part of complexes)
680 demonstrates a high affinity to adsorb hydrogen atoms [77]. Consequently, the presence of
681 interstitial Ag impurities significantly increases the magnitude of negative formation energies for
682 the intermediate steps in the FA oxidation reaction (Figure 11). Note that some of the FA oxidation
683 steps (e.g., the second (Equation 11) and third (Equation 12) steps) on both the reduced and non-
684 reduced substrates are endothermic (Figure 11). As the magnitude of the energy cost for the
685 endothermic steps is on the order of 0.8 eV, they could be realized at RT with a low yield, which
686 is in line with the observed low Y_{CO2} at relatively low temperatures (see Section 3.2). The
687 exothermic-to-endothermic shift in some stages of the FA oxidation reaction corresponds to
688 hydrogen adsorption on the non-reduced eggshell surface. Hence, an alternative pathway involving
689 the adsorption of the hydrogen atom supplied by FA_{ads} onto the MnO_2 surface was also considered
690 (Figure 10 (c)).

691 Two possible scenarios were checked to evaluate the energetics of hydrogen adsorption onto
692 the MnO_2 surface, namely, the formation of Mn-H and O-H bonds (Figure 10 (c)). As the formation
693 of the O-H bond is more favorable than the Mn-H bond, the modeling for the next stage was
694 considered based only on the former case. The results of theoretical calculations indicate that the
695 endothermic steps of the FA oxidation reaction are transformed into exothermic steps through the
696 adsorption of hydrogen onto the MnO_2 co-catalyst (Figure 11). Another possible effect of the
697 MnO_2 co-catalyst is on the capture and activation of O_2. The activation of O_2 could be realized as
698 the O=O → -O-O- reaction or as the transition of the oxygen from the ground (triplet) to the excited
699 state (singlet). In the gas phase, the energy cost of the triplet-singlet O_2 transition is ~ 1.2 eV. The
700 theoretical calculations demonstrate that O_2 adsorption onto MnO_2 is energetically favorable (~ -

70 kJ mol^{-1}). The O_2 molecule is then spontaneously transitioned into the singlet state. Thus, the MnO_2 co-catalyst helps enhance the catalytic activity by effectively capturing and activating O_2 for the FA oxidation reaction. Note that hydrogen chemisorption and O_2 physisorption, followed by their activation, alters the Mulliken occupancy of the 3d shells in the surface Mn atoms. The above observation qualitatively agrees with the results of experimental XPS measurements (see Sections 3.1.2 and 3.3.1).

In the last step of the theoretical modeling, the effect of the hydrogenation of the doped (001) $CaCO_3$ surface on the FA oxidation process was analyzed (Figure 10 (b)). The simulation results indicate that the reduction pre-treatment enhances the catalytic activity of the doped eggshell substrates for the FA oxidation reaction. The above observation is in qualitative agreement with the experimental results (see Section 3.2). Note that Ag^0 demonstrates a strong affinity for hydrogenation, similar to other transitional metals. In summary, the theoretical DFT modeling demonstrates that the Ag catalyst and MnO_2 co-catalyst should create synergetic effects to enhance the efficiency of FA oxidation over the eggshell catalysts when combined with reduction pre-treatment (in line with the experimental observations). As various synergistic processes can occur concurrently on eggshell, Ag, and MnO_2 surface sites, it is not simple enough to pinpoint a specific rate-determining step. Nevertheless, the FA oxidation process on the Ag-MnO_2/Eggshell catalyst can be assumed to occur through the Mars-Van Krevelen (MvK)-type mechanism (based on the FA oxidation pathway simulated through DFT), as is commonly observed for various gas-phase oxidation reactions [78-80]. The interaction between the FA_{ads} and O* species is often the rate-determining step in the MvK mechanism [78, 79].

4. FA oxidation performance comparison

To compare the DLT FA oxidation performance of Ag-1.5%-MnO_2/Eggshell-R with other supported Ag catalysts reported in the literature, the steady-state r-value derived at 80°C was utilized as the relevant performance metric (Table 2). Note that the steady-state r-value has been typically utilized in the literature to compare the performances of thermocatalysts as it incorporates the critical process variables and parameters (X_{FA}, V_{FA}, and m_{cat}) in its derivation [11, 32]. Also, a normalized r-value (per unit Ag (wt.%)) was derived to compare the performances of the reported catalysts more meaningfully by including their respective Ag loadings (Table 2).

As observed from Table 2, the r-value (at 80°C) ranged from 9.4 mmol g^{-1} h^{-1} (Ag-1.5%-MnO_2/Eggshell-R) to 99 mmol g^{-1} h^{-1} (Ag/cerium(IV) oxide (CeO_2)) [81]. However, to obtain higher catalytic activities for FA oxidation, the Ag loadings reported in the literature varied between 0.1-8 wt.%, which is a fairly large range and is unfavorable from an economic perspective (Table 2). In terms of the normalized r-values, Ag-1.5%-MnO_2/Eggshell-R was the best performer for the DLT FA oxidation reaction (1,806 mmol g^{-1} h^{-1} (Ag (wt.%))$^{-1}$) followed by Ag-0.9%-K/MnO_2 (442 mmol g^{-1} h^{-1} (Ag (wt.%))$^{-1}$) [18] (Table 2).

As Ag-1.5%-MnO_2/Eggshell-R only contains 1.1 wt.% Mn, it is much more practical than Ag-0.9%-K/MnO_2 (second-best performer in terms of the normalized r-value) which uses MnO_2 as the support itself [18] (Table S1). The eggshell support utilized in this work is a readily available biowaste whose utilization offers a win-win alternative for simultaneous air quality and solid waste management. Furthermore, the utilization of eggshell biowaste in the synthesis of Ag-1.5%-MnO_2/Eggshell offers a practical solution for meeting goals associated with the circular economy and sustainability [82, 83]. Due to the minuscule metal content in Ag-1.5%-MnO_2/Eggshell (Ag and Mn wt.% of 0.03 and 1.1, respectively), this catalyst results in very low environmental concern from an overall lifecycle assessment perspective [82] (Table S1). Overall, Ag-1.5%-

747 MnO_2/Eggshell-R appears to be one of the best-performing catalysts for the DLT FA oxidation
748 reaction in terms of both the absolute performance (normalized r-value) and sustainability.

749

750 **5. Conclusions**

751 In this work, we report the deep oxidation of FA under DLT conditions using Ag-
752 MnO_2/Eggshell catalysts with ultralow noble metal content. Specifically, 0.03%-Ag-(0.5-5%)-
753 MnO_2/Eggshell catalysts were prepared and employed for DLT-oxidation of FA. The T_{90} of 100
754 ppm FA varied as follows (GHSV of 5,308 h^{-1}): Ag/Eggshell-R (175°C) > Ag-0.5%-
755 MnO_2/Eggshell-R (123°C) > Ag-5%-MnO_2/Eggshell-R (113°C) > MnO_2-R (99°C) > Ag-1.5%-
756 MnO_2/Eggshell (96°C) > Ag-3%-MnO_2/Eggshell-R (93°C) > Ag-1.5%-MnO_2/Eggshell-R (77°C).
757 The T_{90} value (97°C) of a $CaCO_3$ control sample indicates the superiority of the eggshell waste
758 support for the FA oxidation reaction, probably due to the presence of defects in the structure. The
759 best-performing catalyst in this study (Ag-1.5%-MnO_2/Eggshell-R) was then utilized to study the
760 effect of process variables (e.g., FA concentration, flow rate, m_{cat}, and RH) on the FA oxidation
761 performance. The *in-situ* DRIFTS suggest the formation of $HCOO^-$ and CO as the critical
762 intermediates during the FA oxidation reaction. The DFT simulations provided further insights
763 into the FA reaction pathways, surface phenomena, and associated mechanisms. The present study
764 offers intriguing insights into high-performing catalysts with ultralow noble metal content for the
765 FA oxidation reaction under DLT conditions. The utilization of eggshell biowaste offers a unique
766 win-win solution for simultaneous air quality and solid waste management serving the overall
767 objective of meeting circular economy goals and obtaining sustainability.

768

Acknowledgements

This work was supported by a grant from the National Research Foundation of Korea (NRF) funded by the Ministry of Science and ITC (MSIT) of the Korean government (Grant No: 2021R1A3B1068304). P.M.H. would like to thank the Research and Development Program of Ghent University Global Campus (GUGC), Korea.

References

[1] V. Soni, P. Singh, V. Shree, V. Goel, Effects of VOCs on Human Health, in: N. Sharma, A.K. Agarwal, P. Eastwood, T. Gupta, A.P. Singh (Eds.) Air Pollution and Control, Springer Singapore, Singapore, 2018, pp. 119-142.
[2] Z. Rouf, I.Y. Dar, M. Javaid, M.Y. Dar, A. Jehangir, Volatile Organic Compounds Emission from Building Sector and Its Adverse Effects on Human Health, in: J.A. Malik, S. Marathe (Eds.) Ecological and Health Effects of Building Materials, Springer International Publishing, Cham, 2022, pp. 67-86.
[3] Y. Li, B. Yan, Human health risk assessment and distribution of VOCs in a chemical site, Weinan, China, Open Chemistry, 20 (2022) 192-203.
[4] G. Manjunath, R.V. Vardhan, L.L. Praveen, P. Nagaraju, S. Mandal, Room-temperature detection of ammonia and formaldehyde gases by $La_xBa_{1-x}SnO_{3-\delta}$ (x = 0 and 0.05) screen printed sensors: effect of ceria and ruthenate sensitization, Applied Physics A, 127 (2021) 116.
[5] M. Jalali, S.R. Moghadam, M. Baziar, G. Hesam, Z. Moradpour, H.R. Zakeri, Occupational exposure to formaldehyde, lifetime cancer probability, and hazard quotient in pathology lab employees in Iran: a quantitative risk assessment, Environmental Science and Pollution Research, 28 (2021) 1878-1888.
[6] S. Dugheri, D. Massi, N. Mucci, G. Marrubini, G. Cappelli, A. Speltini, M.C. Bonferoni, G. Arcangeli, Exposure to airborne formaldehyde: Sampling and analytical methods—A review, Trends in Environmental Analytical Chemistry, 29 (2021) e00116.
[7] C. He, J. Cheng, X. Zhang, M. Douthwaite, S. Pattisson, Z. Hao, Recent Advances in the Catalytic Oxidation of Volatile Organic Compounds: A Review Based on Pollutant Sorts and Sources, Chemical Reviews, 119 (2019) 4471-4568.
[8] K. Vellingiri, K. Vikrant, V. Kumar, K.-H. Kim, Advances in thermocatalytic and photocatalytic techniques for the room/low temperature oxidative removal of formaldehyde in air, Chemical Engineering Journal, 399 (2020) 125759.
[9] J. Ye, Y. Yu, J. Fan, B. Cheng, J. Yu, W. Ho, Room-temperature formaldehyde catalytic decomposition, Environmental Science: Nano, 7 (2020) 3655-3709.
[10] J. Guo, C. Lin, C. Jiang, P. Zhang, Review on noble metal-based catalysts for formaldehyde oxidation at room temperature, Applied Surface Science, 475 (2019) 237-255.

[11] K. Vikrant, S. Weon, K.-H. Kim, M. Sillanpää, Platinized titanium dioxide (Pt/TiO_2) as a multi-functional catalyst for thermocatalysis, photocatalysis, and photothermal catalysis for removing air pollutants, Applied Materials Today, 23 (2021) 100993.
[12] L. Miao, J. Wang, P. Zhang, Review on manganese dioxide for catalytic oxidation of airborne formaldehyde, Applied Surface Science, 466 (2019) 441-453.
[13] Y. Guo, D.-P. Yang, M. Liu, X. Zhang, Y. Chen, J. Huang, Q. Li, R. Luque, Enhanced catalytic benzene oxidation over a novel waste-derived Ag/eggshell catalyst, Journal of Materials Chemistry A, 7 (2019) 8832-8844.
[14] X. Chen, H. Wang, M. Chen, X. Qin, H. He, C. Zhang, Co-function mechanism of multiple active sites over Ag/TiO_2 for formaldehyde oxidation, Applied Catalysis B: Environmental, 282 (2021) 119543.
[15] Q. Qi, W. Zhang, Y. Zhang, G. Bai, S. Wang, P. Liang, Formaldehyde oxidation at room temperature over layered MnO_2, Catalysis Communications, 153 (2021) 106293.
[16] M. Wang, L. Zhang, W. Huang, T. Xiu, C. Zhuang, J. Shi, The catalytic oxidation removal of low-concentration HCHO at high space velocity by partially crystallized mesoporous MnO_x, Chemical Engineering Journal, 320 (2017) 667-676.
[17] S. Mo, Q. Zhang, J. Li, Y. Sun, Q. Ren, S. Zou, Q. Zhang, J. Lu, M. Fu, D. Mo, J. Wu, H. Huang, D. Ye, Highly efficient mesoporous MnO_2 catalysts for the total toluene oxidation: Oxygen-Vacancy defect engineering and involved intermediates using in situ DRIFTS, Applied Catalysis B: Environmental, 264 (2020) 118464.
[18] S. Lu, X. Wang, Q. Zhu, C. Chen, X. Zhou, F. Huang, K. Li, L. He, Y. Liu, F. Pang, $Ag–K/MnO_2$ nanorods as highly efficient catalysts for formaldehyde oxidation at low temperature, RSC Advances, 8 (2018) 14221-14228.
[19] B. Bai, Q. Qiao, H. Arandiyan, J. Li, J. Hao, Three-Dimensional Ordered Mesoporous MnO_2-Supported Ag Nanoparticles for Catalytic Removal of Formaldehyde, Environmental Science & Technology, 50 (2016) 2635-2640.
[20] J.A. Bennett, K. Wilson, A.F. Lee, Catalytic applications of waste derived materials, Journal of Materials Chemistry A, 4 (2016) 3617-3637.
[21] M. Baláž, E.V. Boldyreva, D. Rybin, S. Pavlović, D. Rodríguez-Padrón, T. Mudrinić, R. Luque, State-of-the-Art of Eggshell Waste in Materials Science: Recent Advances in Catalysis, Pharmaceutical Applications, and Mechanochemistry, Frontiers in Bioengineering and Biotechnology, 8 (2021).
[22] Y. Guo, Y. Sun, D.-P. Yang, J. Dai, Z. Liu, Y. Chen, J. Huang, Q. Li, Biogenic $Pt/CaCO_3$ Nanocomposite as a Robust Catalyst toward Benzene Oxidation, ACS Applied Materials & Interfaces, 12 (2020) 2469-2480.
[23] Z. Li, D.-P. Yang, Y. Chen, Z. Du, Y. Guo, J. Huang, Q. Li, Waste eggshells to valuable $Co_3O_4/CaCO_3$ materials as efficient catalysts for VOCs oxidation, Molecular Catalysis, 483 (2020) 110766.
[24] H. Huang, J. Dai, X. Liu, K.B. Tan, J. Huang, G. Zhan, Q. Li, Waste Eggshell with naturally-functionalized sulfonic groups as excellent support for loading Pd and Ag nanoparticles towards enhanced 1,3-butadiene hydrogenation, Molecular Catalysis, 510 (2021) 111689.
[25] A. Mittal, M. Teotia, R.K. Soni, J. Mittal, Applications of egg shell and egg shell membrane as adsorbents: A review, Journal of Molecular Liquids, 223 (2016) 376-387.
[26] K. Vikrant, K.-H. Kim, F. Dong, D.W. Boukhvalov, W. Choi, Deep oxidation of gaseous formaldehyde at room-temperature by a durable catalyst formed through the controlled addition of potassium to platinum supported on waste eggshell, Chemical Engineering Journal, 428 (2022) 131177.
[27] P. Munnik, P.E. de Jongh, K.P. de Jong, Recent Developments in the Synthesis of Supported Catalysts, Chemical Reviews, 115 (2015) 6687-6718.
[28] M. Zhang, B. Huang, H. Jiang, Y. Chen, Metal-organic framework loaded manganese oxides as efficient catalysts for low-temperature selective catalytic reduction of NO with NH_3, Frontiers of Chemical Science and Engineering, 11 (2017) 594-602.

[29] A. Kumar, A.S.K. Sinha, Comparative study of hydrogen production from steam reforming of acetic acid over synthesized catalysts via MOF and wet impregnation methods, International Journal of Hydrogen Energy, 45 (2020) 11512-11526.
[30] Z. Li, L. Yu, C. Milligan, T. Ma, L. Zhou, Y. Cui, Z. Qi, N. Libretto, B. Xu, J. Luo, E. Shi, Z. Wu, H. Xin, W.N. Delgass, J.T. Miller, Y. Wu, Two-dimensional transition metal carbides as supports for tuning the chemistry of catalytic nanoparticles, Nature Communications, 9 (2018) 5258.
[31] M.-J. Yoo, S.-H. Jo, K.-H. Kim, An advanced technique for rapid and accurate monitoring of gaseous formaldehyde using large-volume injection interfaced with gas chromatograph/barrier discharge ionization detector (LVI/GC/BID), Microchemical Journal, 147 (2019) 806-812.
[32] Y. Guo, M. Wen, G. Li, T. An, Recent advances in VOC elimination by catalytic oxidation technology onto various nanoparticles catalysts: a critical review, Applied Catalysis B: Environmental, 281 (2021) 119447.
[33] Y. Jian, M. Ma, C. Chen, C. Liu, Y. Yu, Z. Hao, C. He, Tuning the micromorphology and exposed facets of MnO_x promotes methyl ethyl ketone low-temperature abatement: boosting oxygen activation and electron transmission, Catalysis Science & Technology, 8 (2018) 3863-3875.
[34] H. Wu, J. Wang, R. Chen, C. Yuan, J. Zhang, Y. Zhang, J. Sheng, F. Dong, Zn-doping mediated formation of oxygen vacancies in SnO_2 with unique electronic structure for efficient and stable photocatalytic toluene degradation, Chinese Journal of Catalysis, 42 (2021) 1195-1204.
[35] J.M. Soler, E. Artacho, J.D. Gale, A. García, J. Junquera, P. Ordejón, D. Sánchez-Portal, The SIESTA method for ab initio order-N materials simulation, Journal of Physics: Condensed Matter, 14 (2002) 2745-2779.
[36] J.P. Perdew, K. Burke, M. Ernzerhof, Generalized Gradient Approximation Made Simple, Physical Review Letters, 77 (1996) 3865-3868.
[37] M. Dion, H. Rydberg, E. Schröder, D.C. Langreth, B.I. Lundqvist, Van der Waals Density Functional for General Geometries, Physical Review Letters, 92 (2004) 246401.
[38] N. Troullier, J.L. Martins, Efficient pseudopotentials for plane-wave calculations, Physical Review B, 43 (1991) 1993-2006.
[39] K. Vikrant, D.-H. Lim, S.A. Younis, K.-H. Kim, An efficient strategy for the enhancement of adsorptivity of microporous carbons against gaseous formaldehyde: Surface modification with aminosilane adducts, Science of The Total Environment, 743 (2020) 140761.
[40] D.A. Giannakoudakis, V. Nair, A. Khan, E.A. Deliyanni, J.C. Colmenares, K.S. Triantafyllidis, Additive-free photo-assisted selective partial oxidation at ambient conditions of 5-hydroxymethylfurfural by manganese (IV) oxide nanorods, Applied Catalysis B: Environmental, 256 (2019) 117803.
[41] Q. Yang, Q. Li, L. Li, Y. Peng, D. Wang, Y. Ma, J. Li, Synthesis of α–MnO_2–like rod catalyst using YMn_2O_5 A–site sacrificial strategy for efficient benzene oxidation, Journal of Hazardous Materials, 403 (2021) 123811.
[42] J. Liu, L. Lan, X. Liu, X. Yang, X. Wu, Facile synthesis of agglomerated Ag–Pd bimetallic dendrites with performance for hydrogen generation from formic acid, International Journal of Hydrogen Energy, 46 (2021) 6395-6403.
[43] Y. Liu, H. Zhou, R. Cao, X. Liu, P. Zhang, J. Zhan, L. Liu, Facile and green synthetic strategy of birnessite-type MnO_2 with high efficiency for airborne benzene removal at low temperatures, Applied Catalysis B: Environmental, 245 (2019) 569-582.
[44] D.L. Graf, Crystallographic tables for the rhombohedral carbonates, American Mineralogist, 46 (1961) 1283-1316.
[45] K. Vikrant, K.-H. Kim, V. Kumar, D.A. Giannakoudakis, D.W. Boukhvalov, Adsorptive removal of an eight-component volatile organic compound mixture by Cu-, Co-, and Zr-metal-organic frameworks: Experimental and theoretical studies, Chemical Engineering Journal, 397 (2020) 125391.

[46] D.A. Giannakoudakis, Y. Hu, M. Florent, T.J. Bandosz, Smart textiles of MOF/g-C_3N_4 nanospheres for the rapid detection/detoxification of chemical warfare agents, Nanoscale Horizons, 2 (2017) 356-364.
[47] L.d.S. Castro, A.G. Barañano, C.J.G. Pinheiro, L. Menini, P.F. Pinheiro, Biodiesel production from cotton oil using heterogeneous CaO catalysts from eggshells prepared at different calcination temperatures, Green Processing and Synthesis, 8 (2019) 235-244.
[48] J. Jia, P. Zhang, L. Chen, The effect of morphology of α-MnO_2 on catalytic decomposition of gaseous ozone, Catalysis Science & Technology, 6 (2016) 5841-5847.
[49] B. Deljoo, H. Tan, S.L. Suib, M. Aindow, Thermally activated structural transformations in manganese oxide nanoparticles under air and argon atmospheres, Journal of Materials Science, 55 (2020) 7247-7258.
[50] M. Thommes, K. Kaneko, A.V. Neimark, J.P. Olivier, F. Rodriguez-Reinoso, J. Rouquerol, K.S.W. Sing, Physisorption of gases, with special reference to the evaluation of surface area and pore size distribution (IUPAC Technical Report), Pure and Applied Chemistry, 87 (2015) 1051-1069.
[51] M. Kruk, M. Jaroniec, Gas Adsorption Characterization of Ordered Organic−Inorganic Nanocomposite Materials, Chemistry of Materials, 13 (2001) 3169-3183.
[52] E. Bombik, A. Bombik, K. Rymuza, The influence of environmental pollution with fluorine compounds on the level of fluoride in soil, feed and eggs of laying hens in Central Pomerania, Poland, Environmental Monitoring and Assessment, 192 (2020) 178.
[53] W. You, Y. Weng, X. Wang, Z. Zhuang, Y. Yu, Synthesis and Adsorption Properties of Hierarchically Ordered Nanostructures Derived from Porous CaO Network, ACS Applied Materials & Interfaces, 8 (2016) 33656-33665.
[54] J.S. Markovski, D.D. Marković, V.R. Đokić, M. Mitrić, M.Đ. Ristić, A.E. Onjia, A.D. Marinković, Arsenate adsorption on waste eggshell modified by goethite, α-MnO_2 and goethite/α-MnO_2, Chemical Engineering Journal, 237 (2014) 430-442.
[55] C.S. Gopinath, S.G. Hegde, A.V. Ramaswamy, S. Mahapatra, Photoemission studies of polymorphic $CaCO_3$ materials, Materials Research Bulletin, 37 (2002) 1323-1332.
[56] J. Baltrusaitis, C.R. Usher, V.H. Grassian, Reactions of sulfur dioxide on calcium carbonate single crystal and particle surfaces at the adsorbed water carbonate interface, Physical Chemistry Chemical Physics, 9 (2007) 3011-3024.
[57] H. Xu, Z. Qu, S. Zhao, J. Mei, F. Quan, N. Yan, Different crystal-forms of one-dimensional MnO_2 nanomaterials for the catalytic oxidation and adsorption of elemental mercury, Journal of Hazardous Materials, 299 (2015) 86-93.
[58] L.M. Santos, W.A. Machado, M.D. França, K.A. Borges, R.M. Paniago, A.O.T. Patrocinio, A.E.H. Machado, Structural characterization of Ag-doped TiO_2 with enhanced photocatalytic activity, RSC Advances, 5 (2015) 103752-103759.
[59] S.E. Balaghi, C.A. Triana, G.R. Patzke, Molybdenum-Doped Manganese Oxide as a Highly Efficient and Economical Water Oxidation Catalyst, ACS Catalysis, 10 (2020) 2074-2087.
[60] Y. Wang, L. Li, P. Dai, L. Yan, L. Cao, X. Gu, X. Zhao, Missing-node directed synthesis of hierarchical pores on a zirconium metal–organic framework with tunable porosity and enhanced surface acidity via a microdroplet flow reaction, Journal of Materials Chemistry A, 5 (2017) 22372-22379.
[61] J. Wang, G. Zhang, P. Zhang, Layered birnessite-type MnO_2 with surface pits for enhanced catalytic formaldehyde oxidation activity, Journal of Materials Chemistry A, 5 (2017) 5719-5725.
[62] J. Farjas, P. Roura, Exact analytical solution for the Kissinger equation: Determination of the peak temperature and general properties of thermally activated transformations, Thermochimica Acta, 598 (2014) 51-58.
[63] P.M. Heynderickx, J.W. Thybaut, H. Poelman, D. Poelman, G.B. Marin, The total oxidation of propane over supported Cu and Ce oxides: A comparison of single and binary metal oxides, Journal of Catalysis, 272 (2010) 109-120.

[64] Y.-H. Kim, H.-I. Lee, Redox Property of Transition Metal Oxides in Catalytic Oxidation, Journal of the Korean Industrial and Engineering Chemistry, 10 (1999) 1161-1168.
[65] J.A. Dawson, H. Chen, I. Tanaka, First-Principles Calculations of Oxygen Vacancy Formation and Metallic Behavior at a β-MnO_2 Grain Boundary, ACS Applied Materials & Interfaces, 7 (2015) 1726-1734.
[66] F. Kapteijn, L. Singoredjo, A. Andreini, J.A. Moulijn, Activity and selectivity of pure manganese oxides in the selective catalytic reduction of nitric oxide with ammonia, Applied Catalysis B: Environmental, 3 (1994) 173-189.
[67] S. Fritsch, A. Navrotsky, Thermodynamic Properties of Manganese Oxides, Journal of the American Ceramic Society, 79 (1996) 1761-1768.
[68] K.T. Jacob, A. Kumar, G. Rajitha, Y. Waseda, Thermodynamic Data for Mn_3O_4, Mn_2O_3 and MnO_2, High Temperature Materials and Processes, 30 (2011) 459-472.
[69] S. Vyazovkin, Determining Preexponential Factor in Model-Free Kinetic Methods: How and Why?, Molecules, 26 (2021) 3077.
[70] G.I. Panov, K.A. Dubkov, E.V. Starokon, Active oxygen in selective oxidation catalysis, Catalysis Today, 117 (2006) 148-155.
[71] D. Chen, G. Zhang, M. Wang, N. Li, Q. Xu, H. Li, J. He, J. Lu, Pt/MnO_2 Nanoflowers Anchored to Boron Nitride Aerogels for Highly Efficient Enrichment and Catalytic Oxidation of Formaldehyde at Room Temperature, Angewandte Chemie International Edition, 60 (2021) 6377-6381.
[72] T.J. Bandosz, Exploring the Silent Aspect of Carbon Nanopores, Nanomaterials, 11 (2021) 407.
[73] U.J. Etim, Z. Zhong, Z. Yan, P. Bai, 3. Functional catalysts for catalytic removal of formaldehyde from air Environmental Functional Nanomaterials, in: Q. Wang, Z. Zhong (Eds.) Environmental Functional Nanomaterials, De Gruyter, 2019, pp. 89-126.
[74] C. Zhang, H. He, K.-i. Tanaka, Catalytic performance and mechanism of a Pt/TiO_2 catalyst for the oxidation of formaldehyde at room temperature, Applied Catalysis B: Environmental, 65 (2006) 37-43.
[75] X. Chen, G. He, Y. Li, M. Chen, X. Qin, C. Zhang, H. He, Identification of a Facile Pathway for Dioxymethylene Conversion to Formate Catalyzed by Surface Hydroxyl on TiO_2-Based Catalyst, ACS Catalysis, 10 (2020) 9706-9715.
[76] D. Sun, Y. Le, C. Jiang, B. Cheng, Ultrathin Bi_2WO_6 nanosheet decorated with Pt nanoparticles for efficient formaldehyde removal at room temperature, Applied Surface Science, 441 (2018) 429-437.
[77] Z. Li, J.-Y. Fu, Y. Feng, C.-K. Dong, H. Liu, X.-W. Du, A silver catalyst activated by stacking faults for the hydrogen evolution reaction, Nature Catalysis, 2 (2019) 1107-1114.
[78] E. Genty, S. Siffert, R. Cousin, Investigation of reaction mechanism and kinetic modelling for the toluene total oxidation in presence of CoAlCe catalyst, Catalysis Today, 333 (2019) 28-35.
[79] M. Misono, Chapter 1 - Basis of Heterogeneous Catalysis, in: M. Misono (Ed.) Studies in Surface Science and Catalysis, Elsevier, 2013, pp. 1-23.
[80] J.E. Lee, Y.S. Ok, D.C.W. Tsang, J. Song, S.-C. Jung, Y.-K. Park, Recent advances in volatile organic compounds abatement by catalysis and catalytic hybrid processes: A critical review, Science of The Total Environment, 719 (2020) 137405.
[81] L. Ma, D. Wang, J. Li, B. Bai, L. Fu, Y. Li, Ag/CeO_2 nanospheres: Efficient catalysts for formaldehyde oxidation, Applied Catalysis B: Environmental, 148-149 (2014) 36-43.
[82] D.P. Debecker, K. Kuok Hii, A. Moores, L.M. Rossi, B. Sels, D.T. Allen, B. Subramaniam, Shaping Effective Practices for Incorporating Sustainability Assessment in Manuscripts Submitted to ACS Sustainable Chemistry & Engineering: Catalysis and Catalytic Processes, ACS Sustainable Chemistry & Engineering, 9 (2021) 4936-4940.
[83] S. Mignardi, L. Archilletti, L. Medeghini, C. De Vito, Valorization of Eggshell Biowaste for Sustainable Environmental Remediation, Scientific Reports, 10 (2020) 2436.
[84] X. Tang, J. Chen, Y. Li, Y. Li, Y. Xu, W. Shen, Complete oxidation of formaldehyde over Ag/MnO_x–CeO_2 catalysts, Chemical Engineering Journal, 118 (2006) 119-125.

[85] X. Chen, M. Chen, G. He, F. Wang, G. Xu, Y. Li, C. Zhang, H. He, Specific Role of Potassium in Promoting Ag/Al_2O_3 for Catalytic Oxidation of Formaldehyde at Low Temperature, The Journal of Physical Chemistry C, 122 (2018) 27331-27339.
[86] J. Zhang, Y. Li, Y. Zhang, M. Chen, L. Wang, C. Zhang, H. He, Effect of Support on the Activity of Ag-based Catalysts for Formaldehyde Oxidation, Scientific Reports, 5 (2015) 12950.
[87] C.-C. Ou, C.-H. Chen, T.-S. Chan, C.-S. Chen, S. Cheng, Influence of pretreatment on the catalytic performance of Ag/CeO_2 for formaldehyde removal at low temperature, Journal of Catalysis, 380 (2019) 43-54.
[88] B. Bai, J. Li, Positive Effects of K^+ Ions on Three-Dimensional Mesoporous Ag/Co_3O_4 Catalyst for HCHO Oxidation, ACS Catalysis, 4 (2014) 2753-2762.
[89] Z. Qu, D. Chen, Y. Sun, Y. Wang, High catalytic activity for formaldehyde oxidation of AgCo/APTES@MCM-41 prepared by two steps method, Applied Catalysis A: General, 487 (2014) 100-109.

Tables and Figures

Table 1. FA removal performance of the analyzed catalysts [a].

Order	Catalyst	Catalyst activation	T_{50} (°C)[b]	T_{90} (°C)[c]	Conversion (%) at 80°C	r (mmol g^{-1} h^{-1})[d]
1	Ag/Eggshell-R	Reduction at 300°C using H_2 (10%) + N_2 mixture for 3 h (50 mL min^{-1})	113	175	25	2.6
2	Ag-0.5%-MnO_2/Eggshell-R		94	123	31	3.2
3	Ag-1.5%-MnO_2/Eggshell-R		< 30 (62% X_{FA} at 30°C)	77	92	9.4
4	Ag-3%-MnO_2/Eggshell-R		< 30 (59% X_{FA} at 30°C)	93	79	8.1
5	Ag-5%-MnO_2/Eggshell-R		44	113	71	7.2
6	Ag-1.5%-MnO_2/$CaCO_3$-R		51	97	67	6.8
7	MnO_2-R		68	99	59	6.0
8	Ag-1.5%-MnO_2/Eggshell	Heating at 300°C using N_2 for 3 h (50 mL min^{-1})	< 30 (55% X_{FA} at 30°C)	96	74	7.5

[a] Reactant composition: FA (100 ppm) + air (balance), flow rate: 50 mL min^{-1} (3.4E-09 mol s^{-1}), catalyst mass: 120 mg, and GHSV: 5,308 h^{-1}.

[b] Reaction temperature corresponding to X_{FA} of 50%.

[c] Reaction temperature corresponding to X_{FA} of 90%.

[d] Steady-state reaction rate obtained at 80°C.

re for 1 h followed duction at 200°C g H_2 (10%) + N_2 ixture for 1 h	FA + O_2 (21 vol.%) + N_2 (balance)	300	30	6.1E-09	36,000 mL h^{-1} g^{-1}	< 20 (70% X_{FA} at 20°C)	35	100	44	442	[18]
-	FA + O_2 (20 vol.%) + N_2 (balance)	810	100	5.5E-08	84,000 h^{-1}	90	108	25	99	50	[81]
-	FA + O_2 (18 vol.%) + He (balance)	580	100	4.0E-08	30,000 mL h^{-1} g^{-1}	70	93	70	50	17	[84]
-	FA + O_2 (20 vol.%) + He (balance)	110	100	7.5E-09	100,000 mL h^{-1} g^{-1}	38	54	100	45	5.6	[85]
-	FA + O_2 (20 vol.%) + N_2 (balance)	110	100	7.5E-09	100,000 mL h^{-1} g^{-1}	65	87	85	38	4.8	[86]
-	FA + O_2 (20 vol.%) + N_2 (balance)	110	100	7.5E-09	100,000 mL h^{-1} g^{-1}	73	103	65	29	3.7	[86]
-	FA + O_2 (20 vol.%) + He (balance)	130	100	8.9E-09	100,000 mL h^{-1} g^{-1}	88	212	40	21	2.7	[14]
uction at 300°C g H_2 (10%) + N_2 re for 4 h (50 mL min^{-1})	FA + Air (balance)	400	100	2.7E-08	24,400 h^{-1}	47	59	98	19	3.2	[87]
-	FA + O_2 (20 vol.%) + N_2 (balance)	100	100	6.8E-09	30,000 h^{-1}	< 30 (55% X_{FA} at 30°C)	65	100	12	1.5	[88]
-	FA + O_2 (20 vol.%) + He (balance)	130	100	8.9E-09	100,000 mL h^{-1} g^{-1}	91	110	30	16	2.0	[14]
-	FA + O_2 (20 vol.%) + N_2 (balance)	110	100	7.5E-09	100,000 mL h^{-1} g^{-1}	88	> 125 (75% X_{FA} at 125°C)	40	18	2.2	[86]
itioning at 500°C ing O_2 for 2 h	FA + O_2 (20 vol.%) + Ar (balance)	500	30	1.0E-08	9,000 mL h^{-1} g^{-1}	60	85	84	15	-	[89]
uction at 300°C g H_2 (10%) + N_2 re for 3 h (50 mL min^{-1})	FA + Air (balance)	100	50	3.4E-09	5,308 h^{-1}	< 30 (62% X_{FA} at 30°C)	77	92	9.4	314	This study
uction at 300°C g H_2 (10%) + N_2 re for 3 h (50 mL min^{-1})	FA + Air (balance)	100	500	3.4E-08	53,080 h^{-1}	72	144	53	54	1,806	This study

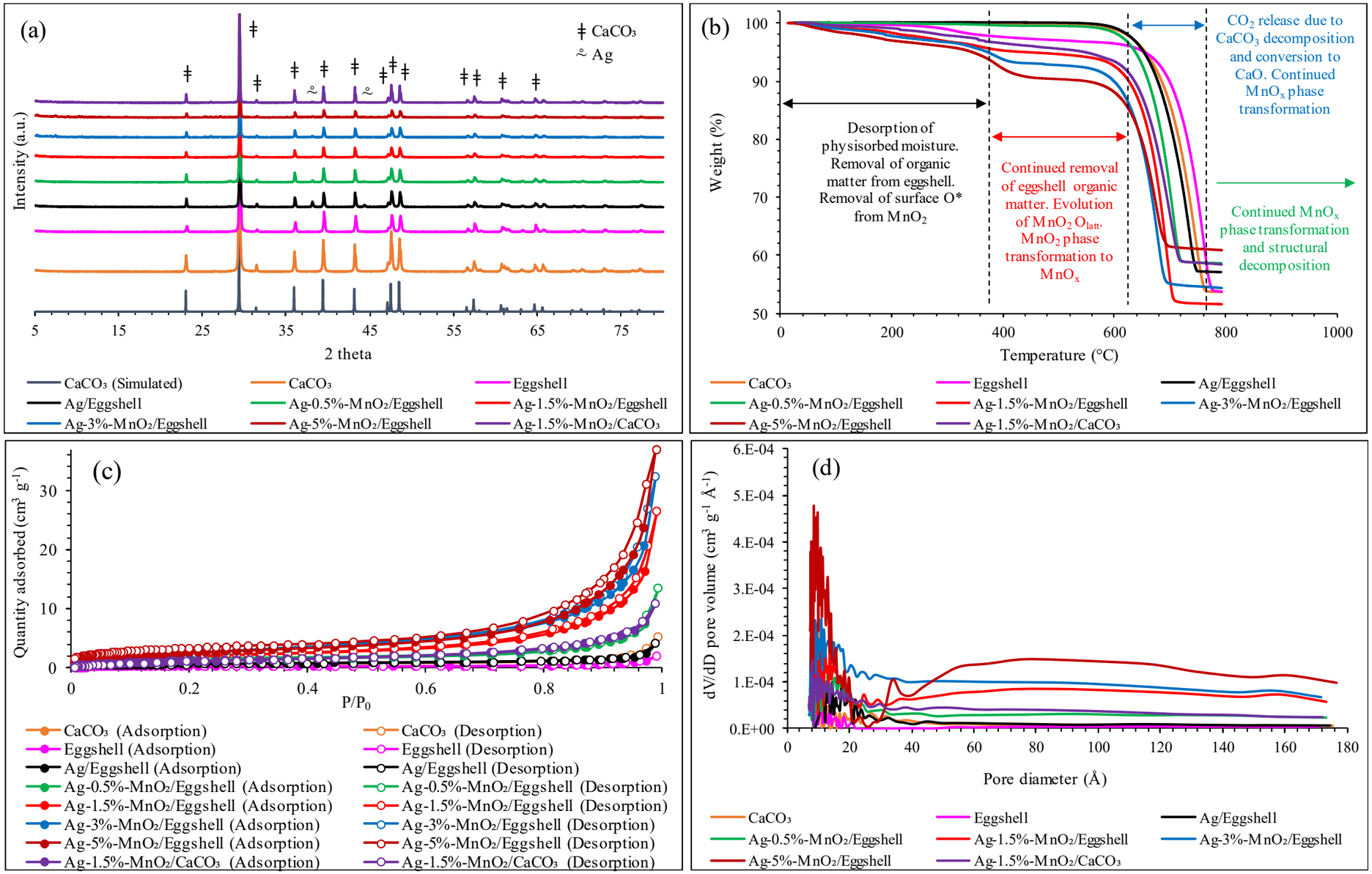

Figure 1. Physicochemical characterization results of $CaCO_3$, eggshell, and Ag-MnO_2/Eggshell composites. (a) PXRD patterns, (b) TGA profiles, (c) N_2 adsorption-desorption isotherms and (d) pore size distributions.

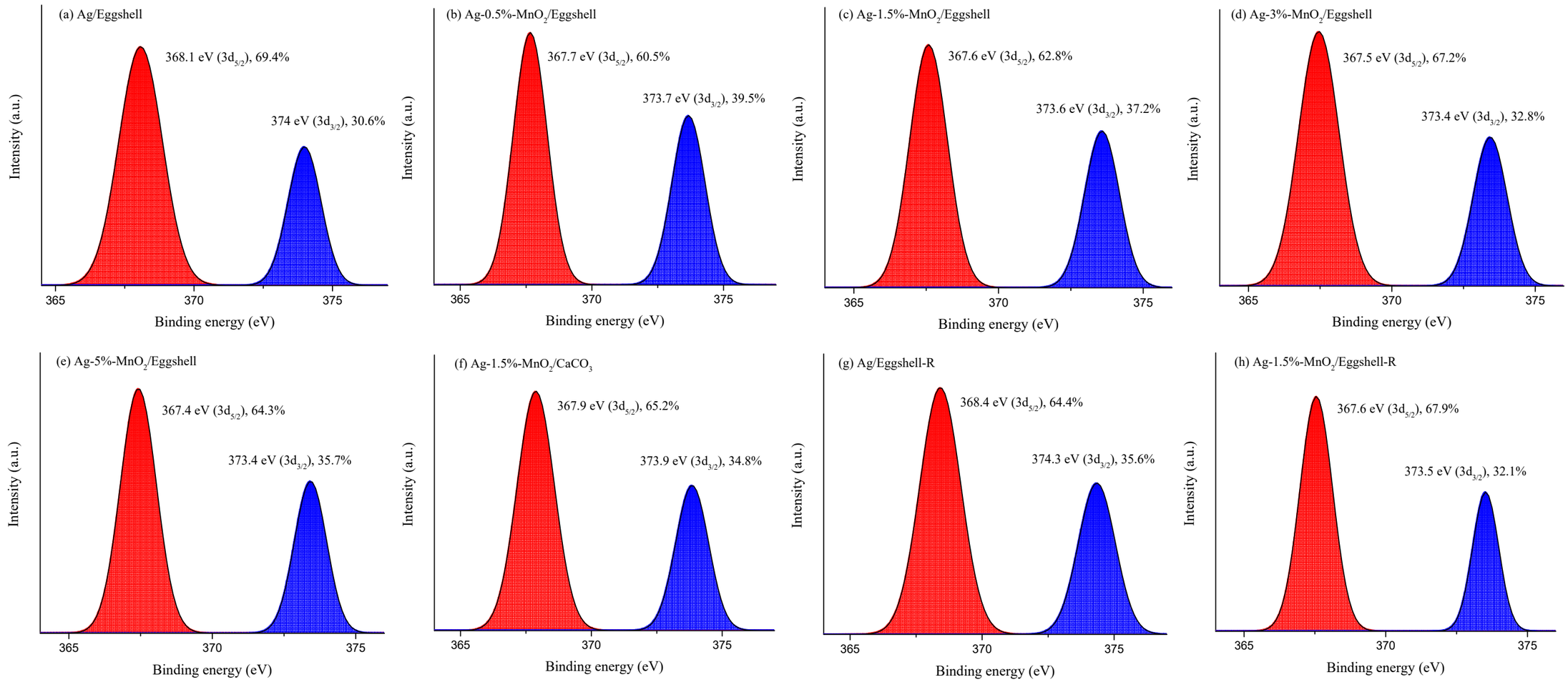

Figure 2. Deconvoluted core level Ag 3d XPS spectra of the analyzed catalysts: (a) Ag/Eggshell, (b) Ag-0.5%-MnO_2/Eggshell, (c) Ag-1.5%-MnO_2/Eggshell, (d) Ag-3%-MnO_2/Eggshell, (e) Ag-5%-MnO_2/Eggshell, (f) Ag-1.5%-MnO_2/$CaCO_3$, (g) Ag/Eggshell-R, and (h) Ag-1.5%-MnO_2/Eggshell-R.

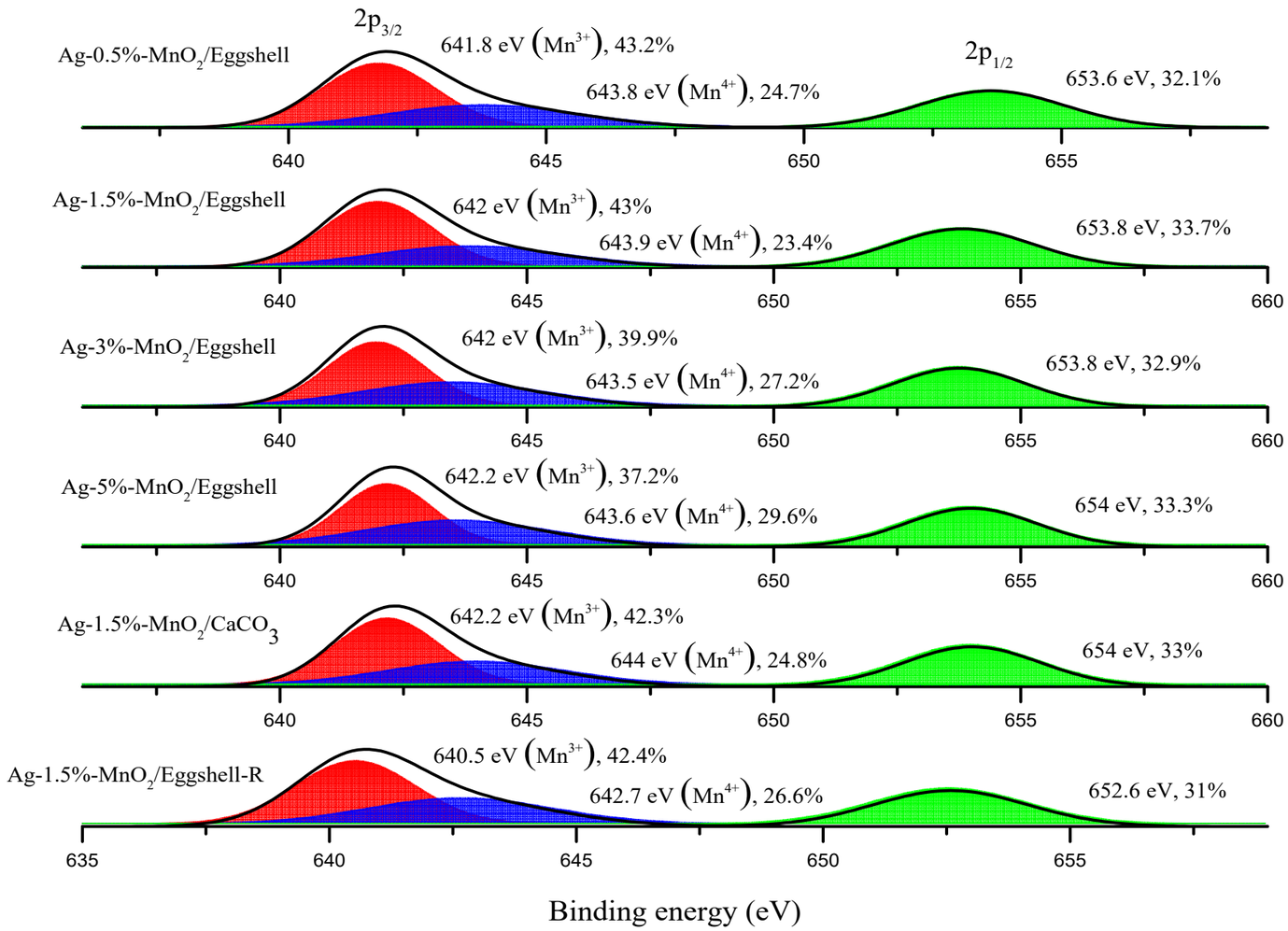

Figure 3. Deconvoluted core level Mn 2p XPS spectra of the analyzed catalysts.

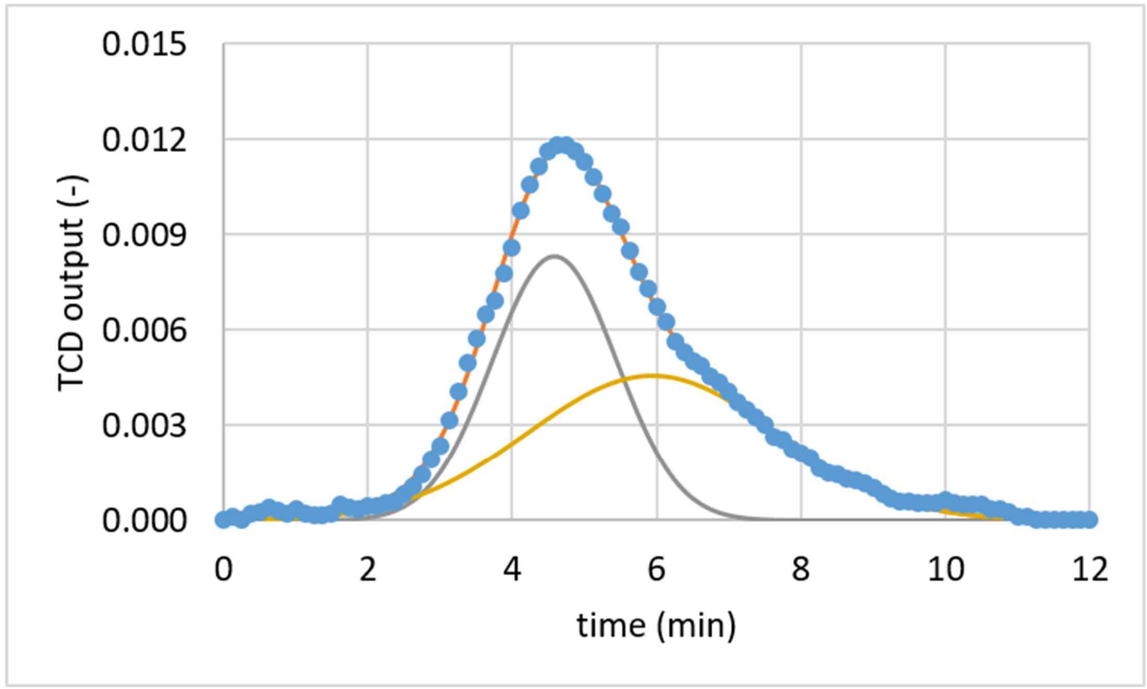

Figure 4. CO-TPD profile (until 383 K) for β = 10 K min^{-1}. (—) peak 1, (—) peak 2, and (—) total calculated signal.

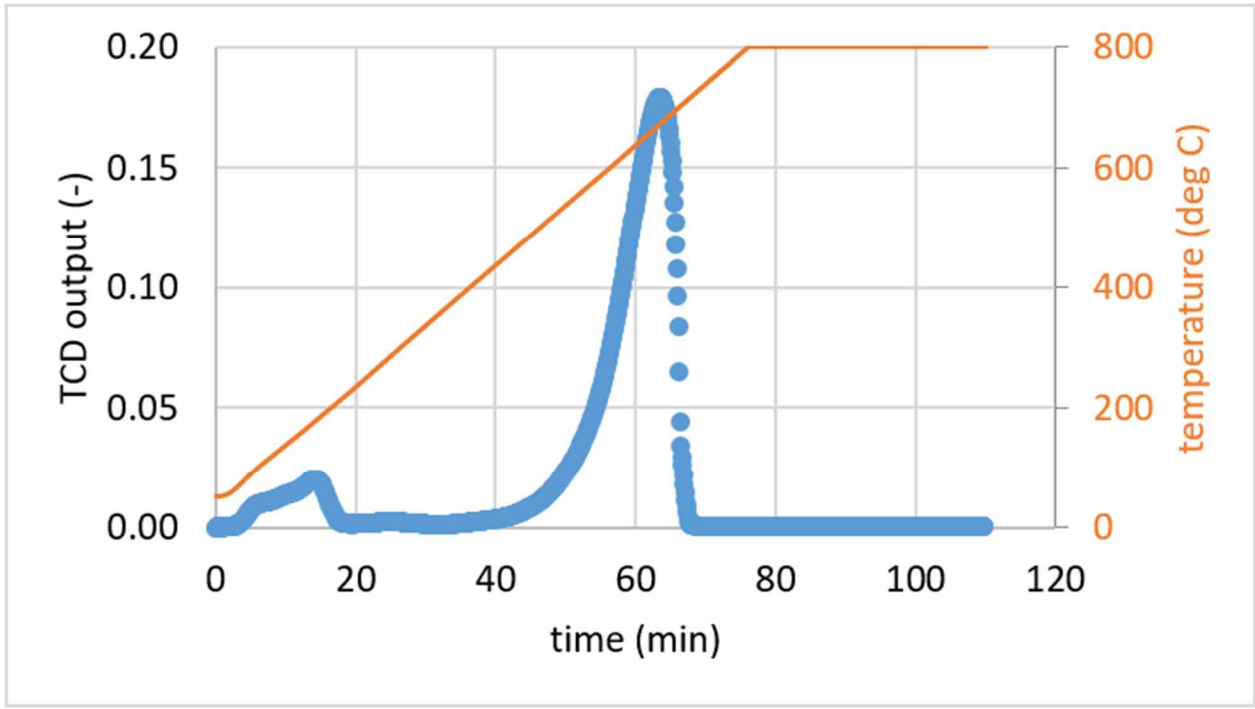

Figure 5. H_2-TPR profile for β = 10 K min^{-1}. (●) TCD output and (—) temperature profile versus time.

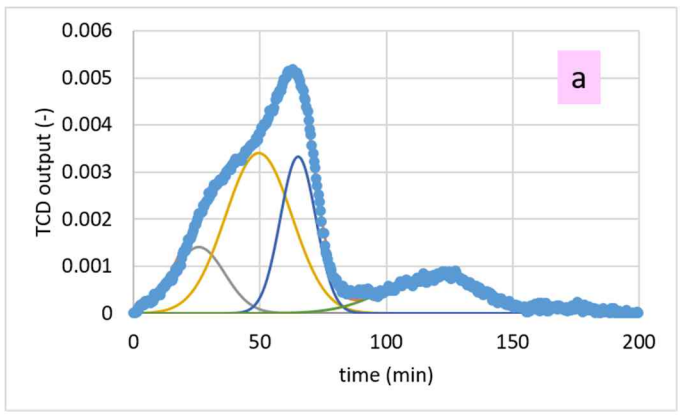

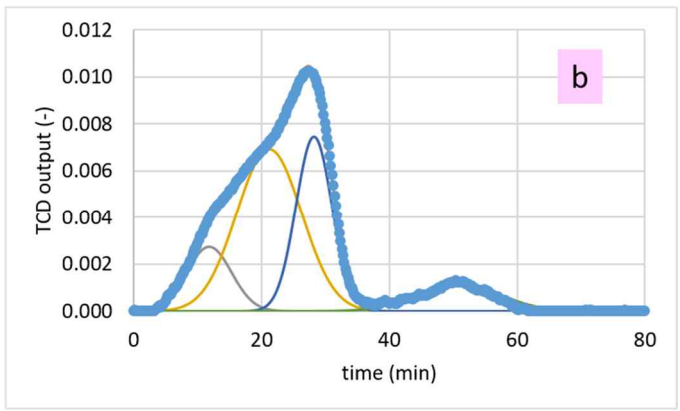

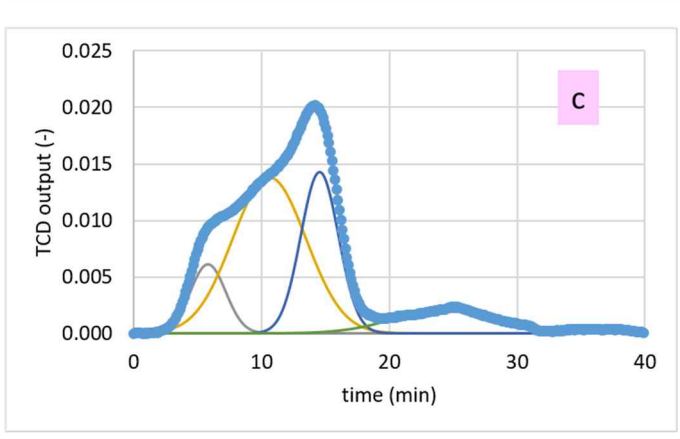

Figure 6. H_2-TPR profile (until 723 K) for (a) $\beta = 2$ K min^{-1}, (b) $\beta = 5$ K min^{-1}, and (c) $\beta = 10$ K min^{-1}. (—) peak 1, (—) peak 2, (—) peak 3, (—) peak 4, and (—) total calculated signal.

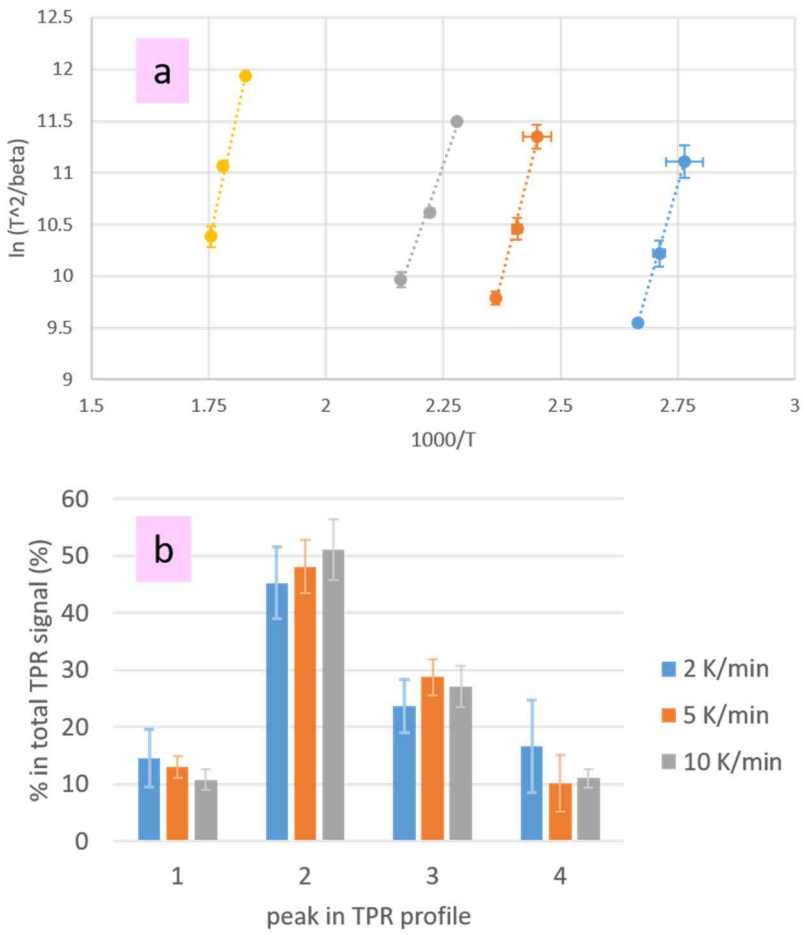

Figure 7. H2-TPR results. (a) Data couples (T_{max}, β) for (●) peak 1, (●) peak 2, (●) peak 3, and (●) peak 4. Dotted lines represent the linear regression per peak. (b) Contribution of the peaks to the total TCD signal. (■) β = 2 K min^{-1}, (■) β = 5 K min^{-1} and (■) β = 10 K min^{-1}.

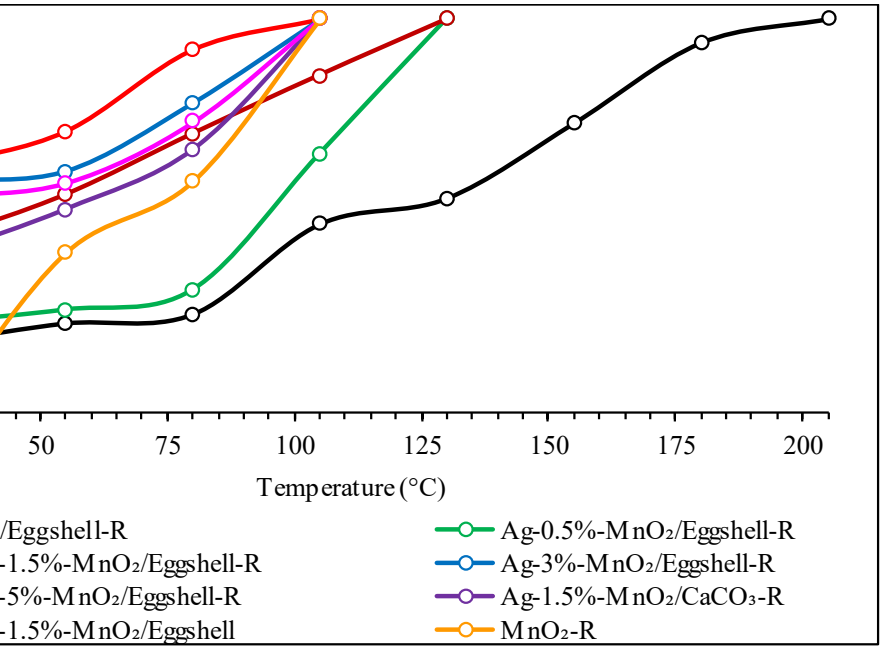
50
75
100
125
150
175
200
Temperature (°C)
/Eggshell-R
-1.5%-MnO2/Eggshell-R
-5%-MnO2/Eggshell-R
-1.5%-MnO2/Eggshell
Ag-0.5%-MnO2/Eggshell-R
Ag-3%-MnO2/Eggshell-R
Ag-1.5%-MnO2/CaCO3-R
MnO2-R

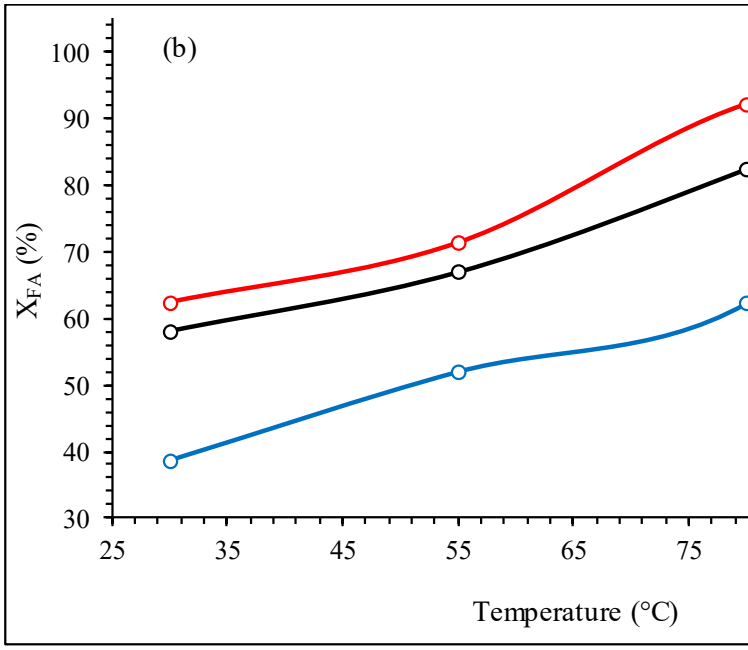
(b)
100
90
80
70
60
50
40
30
XFA (%)
25
35
45
55
65
75
Temperature (°C)

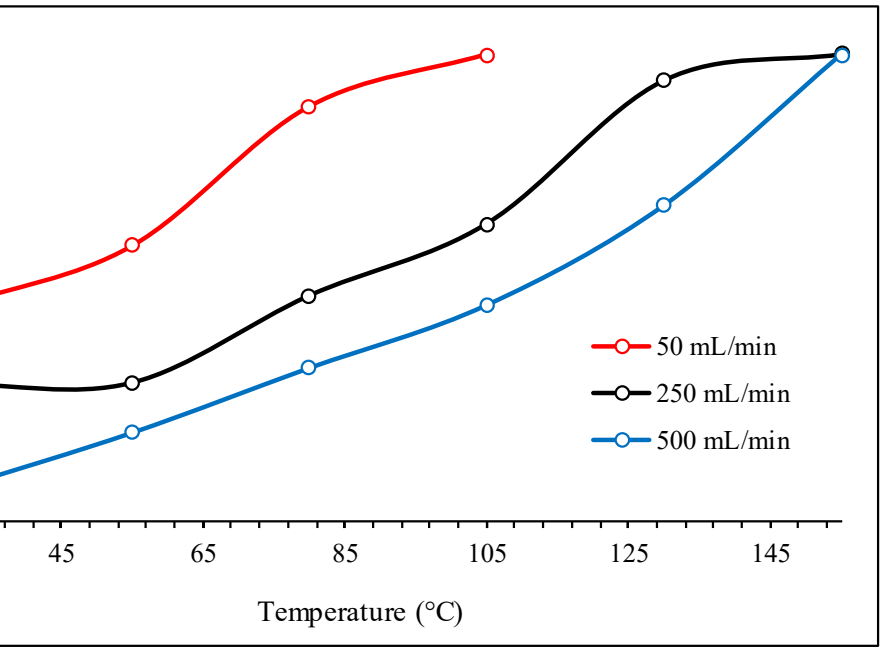
50 mL/min
250 mL/min
500 mL/min
45
65
85
105
125
145
Temperature (°C)

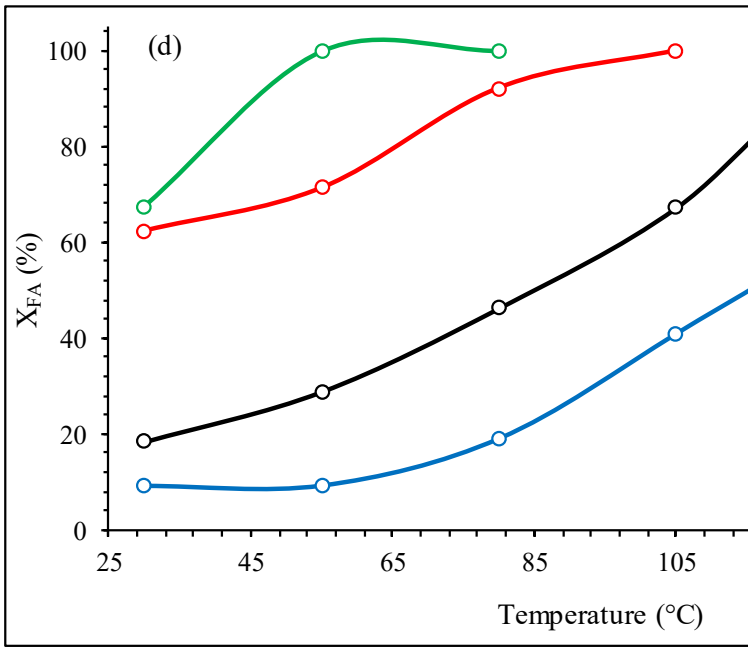
(d)
100
80
60
40
20
0
XFA (%)
25
45
65
85
105
Temperature (°C)

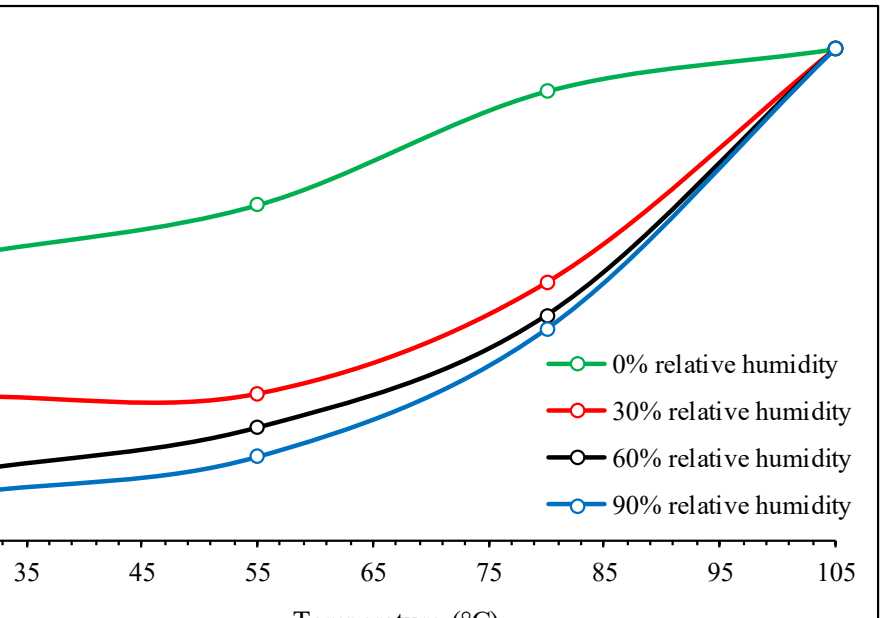
0% relative humidity
30% relative humidity
60% relative humidity
90% relative humidity
35
45
55
65
75
85
95
105

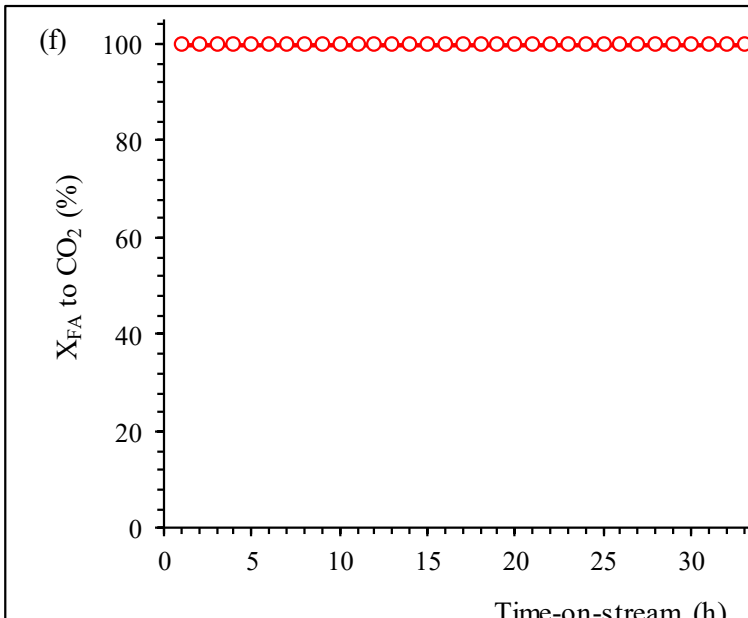
(f)
100
80
60
40
20
0
XFA to CO2 (%)
0
5
10
15
20
25
30
Time-on-stream (h)

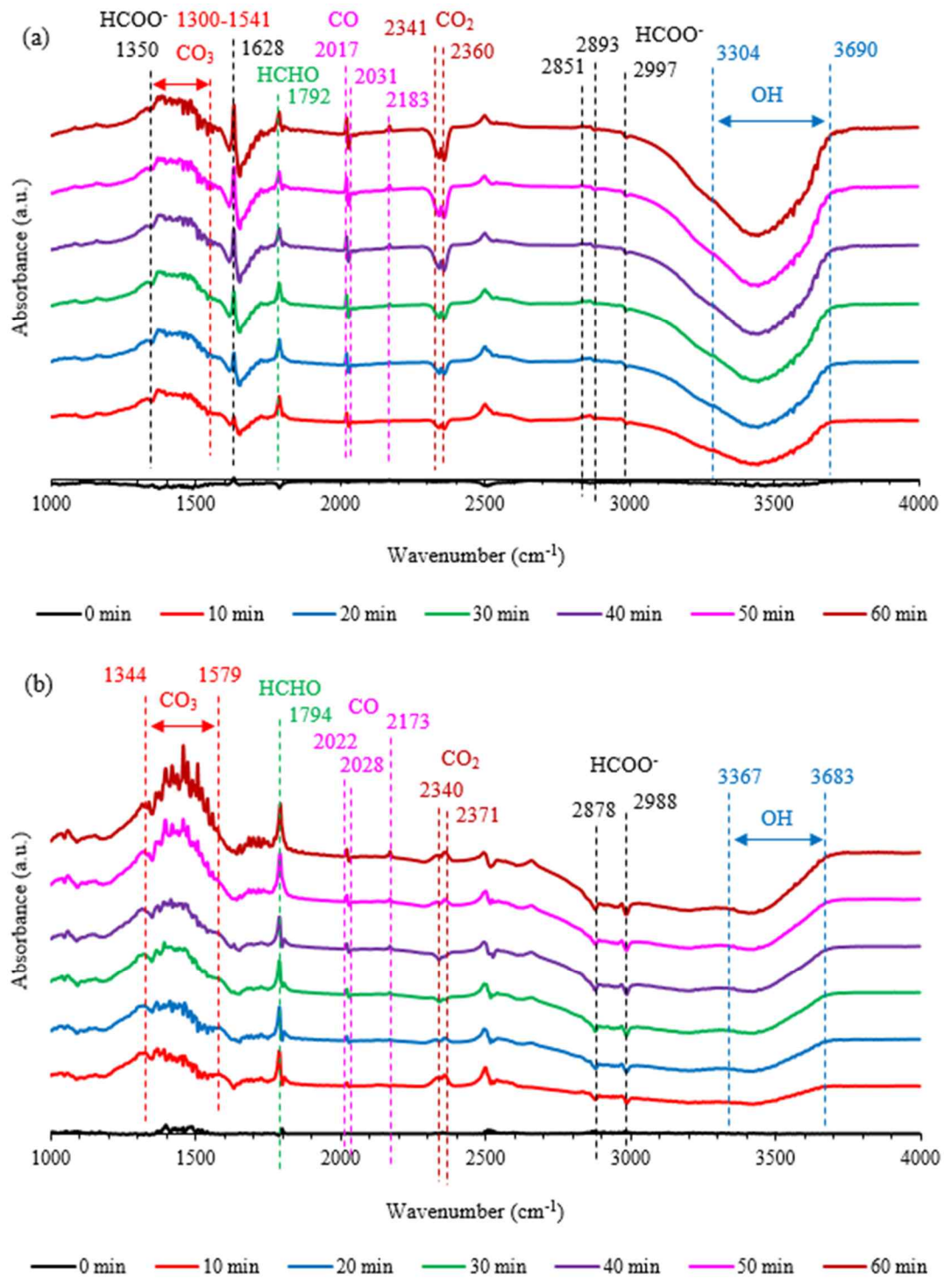

Figure 9. *In-situ* DRIFTS spectrum for a 1:1 FA + O_2 mixture (acquired at 100°C under dark condition), (a) Ag/Eggshell-R and (b) Ag-1.5%-MnO_2/Eggshell-R.

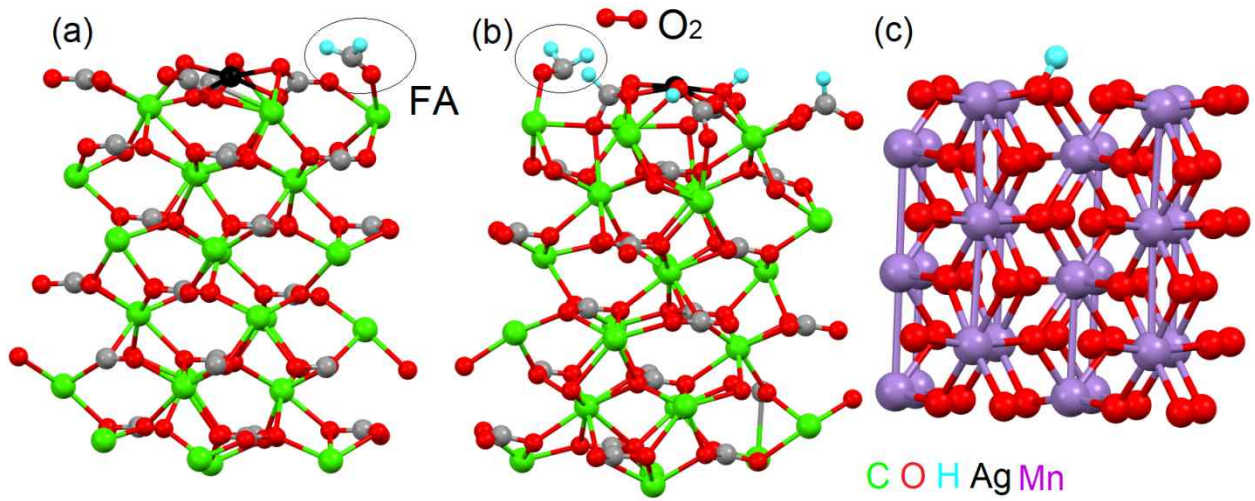

Figure 10. Atomic structures simulated using DFT: (a) optimized atomic structure of the FA molecule physisorbed on the pristine eggshell surface in the vicinity of the interstitial Ag center, (b) optimized atomic structure of the FA molecule physisorbed on the hydrogenated eggshell surface in the vicinity of the interstitial Ag center and the co-presence of O_2, (c) optimized atomic structure of the MnO_2 slab with the chemisorbed hydrogen atom.

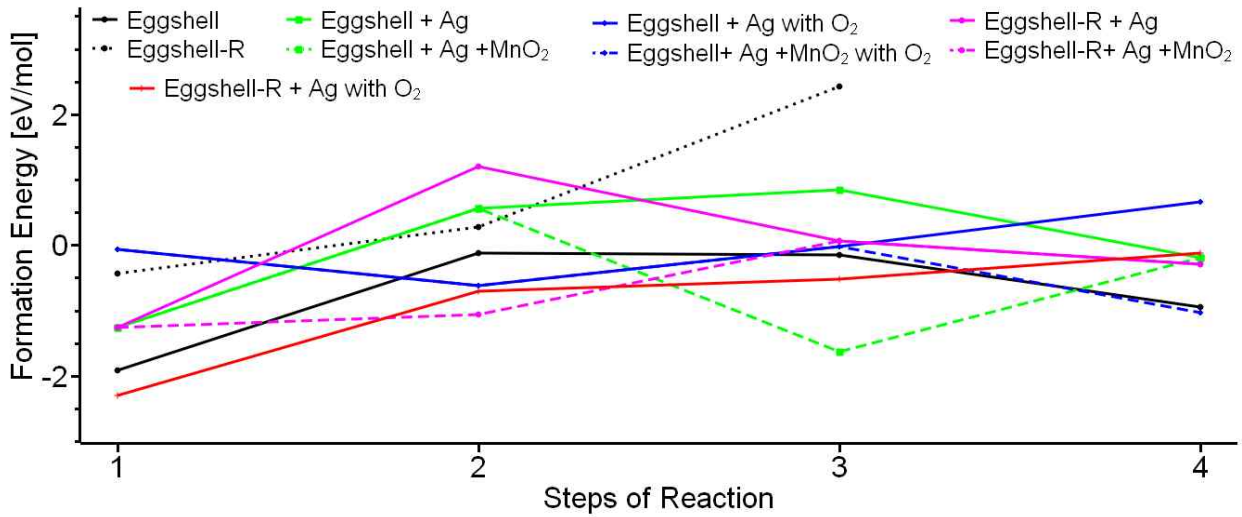

Figure 11. The calculated formation energies of the four-step X_{FA} to CO_2 (Equations 10-13) over the non-modified and modified eggshell surfaces in the absence and presence of O_2.